

# A study of compressibility effects in the high-speed turbulent shear layer using direct simulation

By C. PANTANO AND S. SARKAR

Department of Mechanical and Aerospace Engineering, University of California San Diego,  
9500 Gilman Drive, La Jolla, CA 92093-0411, USA

(Received 25 March 1999 and in revised form 23 July 2001)

Direct simulations of the turbulent shear layer are performed for subsonic to supersonic Mach numbers. Fully developed turbulence is achieved with profiles of mean velocity and turbulence intensities that agree well with laboratory experiments. The thickness growth rate of the shear layer exhibits a large reduction with increasing values of the convective Mach number,  $M_c$ . In agreement with previous investigations, it is found that the normalized pressure–strain term decreases with increasing  $M_c$ , which leads to inhibited energy transfer from the streamwise to cross-stream fluctuations, to the reduced turbulence production observed in DNS, and, finally, to reduced turbulence levels as well as reduced growth rate of the shear layer. An analysis, based on the wave equation for pressure, with supporting DNS is performed with the result that the pressure–strain term decreases monotonically with increasing Mach number. The gradient Mach number, which is the ratio of the acoustic time scale to the flow distortion time scale, is shown explicitly by the analysis to be the key quantity that determines the reduction of the pressure–strain term in compressible shear flows. The physical explanation is that the finite speed of sound in compressible flow introduces a finite time delay in the transmission of pressure signals from one point to an adjacent point and the resultant increase in decorrelation leads to a reduction in the pressure–strain correlation.

The dependence of turbulence intensities on the convective Mach number is investigated. It is found that all components decrease with increasing  $M_c$  and so does the shear stress.

DNS is also used to study the effect of different free-stream densities parameterized by the density ratio,  $s = \rho_2/\rho_1$ , in the high-speed case. It is found that changes in the temporal growth rate of the vorticity thickness are smaller than the changes observed in momentum thickness growth rate. The momentum thickness growth rate decreases substantially with increasing departure from the reference case,  $s = 1$ . The peak value of the shear stress,  $\overline{uw}$ , shows only small changes as a function of  $s$ . The dividing streamline of the shear layer is observed to move into the low-density stream. An analysis is performed to explain this shift and the consequent reduction in momentum thickness growth rate.

---

## 1. Introduction

At high Mach number, the growth of the turbulent shear layer is substantially reduced. This stabilizing effect is one of the most remarkable features distinguishing compressible turbulence from its incompressible counterpart. Moreover, it has

important implications for applications such as scramjet engines and abatement of supersonic jet noise. Observations of the reduced growth rate at high speeds are numerous. Early experimental evidence is discussed by Bradshaw (1977), and Kline, Cantwell & Lilley (1982) while later experimental and numerical investigations are reviewed by Lele (1994) and Smits & Dussauge (1996).

The convective Mach number,  $M_c$ , introduced by Bogdanoff (1983) has become popular as the parameter that determines compressibility effects. Denoting the velocity, density and speed of sound in the high-speed stream by  $U_1, \rho_1, c_1$  and corresponding quantities in the low-speed stream by  $U_2, \rho_2, c_2$  and, assuming equal specific heats, gives  $M_c = (U_1 - U_2)/(c_1 + c_2)$ . From experimental data, see figure 7 for example, it is clear that there is a general trend of decreasing thickness growth rate with increasing values of  $M_c$ . In the case of high-speed propulsion, there is an additional effect, namely, density changes due to changes in composition and heat release. Therefore, the related question of how the density ratio,  $s = \rho_2/\rho_1$ , affects the growth rate is of interest. In the low-speed case, Brown & Roshko (1974) found that the shear layer growth rate shows an increase with increasing density ratio,  $s$ , with a change of approximately 25% from the equal-density case when  $s = 7$  or  $s = 1/7$ . Functional forms for the dependence on  $s$  were proposed by Brown (1974) and Dimotakis (1984) to match the experimental data. Hall, Dimotakis & Rosemann (1993) observed that when the visual thickness growth rate was normalized by the correlation of Dimotakis (1984) applicable to the variable-density low-speed shear layer, quasi-incompressible cases with  $M_c < 0.3$  but with low values of density ratio,  $s = 0.2, 0.1, 0.058$ , have an anomalous reduction with respect to the expected trend. Lu & Lele (1994) performed a spatial stability analysis of the cases considered experimentally by Hall *et al.* (1993) and found that if the ratio of the maximal growth rate, normalized by that of the corresponding variable-density zero-Mach number case, is plotted, the three cases with anomalous behaviour collapse onto the plot determined by the other cases. Evidently, the issue of whether the density ratio has an effect over and above that of the convective Mach number in compressible shear flow requires further study.

Apart from the convective Mach number, there are other relevant Mach numbers: the turbulent Mach number,  $M_t = u/c$  based on r.m.s. velocity,  $u$ , and the gradient Mach number,  $M_g = Sl/c$ , based on the mean velocity gradient,  $S$ , and the length scale,  $l$ , in the direction of the gradient. The parameter  $M_g$  is a ratio of the acoustic time scale,  $l/c$ , to the mean flow distortion time scale,  $1/S$ , and has been used in compressible rapid distortion theory, for example, Cambon, Coleman & Mansour (1993). The gradient Mach number was shown by Sarkar (1995) to be much larger in the shear layer than in the boundary layer at the same mean Mach number, and, therefore, useful in differentiating between the strong compressibility effects in the shear layer and their lack in the boundary layer.

Identification of the mechanisms responsible for the inhibited shear layer growth at high Mach number is of interest both to gain a fundamental understanding of the problem and to derive insights into possible mixing enhancement strategies. Thus, a number of alternative scenarios have been proposed. Linear instability theory predicts a reduction of growth rate with increased convective Mach number,  $M_c$ , and an analogy with linear instability theory has been proposed, for example, by Sandham & Reynolds (1991). The analysis of Balsa & Goldstein (1990) using high-Mach-number asymptotics leads to a simple hypersonic similarity law that explains how spatial and temporal phase speeds and growth rates scale with Mach number.

However, the applicability of linear instability theory to a turbulent, nonlinearly evolving flow is uncertain. The effect of compressibility on large-scale coherent struc-

tures has been studied by Papamoschou & Roshko (1988), Samimy, Reeder & Elliott (1992), Hall *et al.* (1993), and Clemens & Mungal (1995) as a potential mechanism; however definitive and quantitative links to the compressibility effect have not been established.

There are additional terms, compressible dissipation and pressure–dilatation, in the turbulent kinetic energy equation which have been modelled by Zeman (1990), Sarkar *et al.* (1991), Taulbee & VanOsdol (1991), Sarkar (1992) and Ristorcelli (1997). It was proposed that these dilatational terms act as sinks and, for sufficiently large turbulent Mach number, could lead to reduction of the turbulence levels and thereby shear layer thickness. Reduction in turbulence levels was observed by Blaisdell, Mansour & Reynolds (1993) and Sarkar (1995) in simulations of uniformly sheared flow. However, Sarkar (1995) showed that reduced turbulent production is responsible for decreased turbulent kinetic energy and not the dilatational terms. In the shear layer, a direct relationship between the momentum thickness growth rate and the integrated turbulent production was established by Vreman, Sandham & Luo (1996) that showed that a reduction in momentum thickness growth rate is equivalent to that in the integrated production. In two-dimensional simulations of an isolated vortex in a shear layer by Papamoschou & Lele (1993), the Reynolds shear stress associated with the fluctuating disturbance field was found to be significantly reduced. Simone, Coleman & Cambon (1997) also observed reduced production and Reynolds stress in their DNS of uniformly sheared flow. In addition, they performed an instructive analysis based on rapid distortion theory (RDT) that shows reduced production. RDT was found useful for explaining the structural change of pressure and velocity terms under compressibility. The implications of linearized theory for turbulent fluctuations in compressible flow have been further explored by Friedrich & Bertolotti (1997).

Thus, evidence from available studies indicates that the reduction of turbulent kinetic energy in the uniform shear layer as well as the reduced thickness of the shear layer is related to decreased turbulent production. Investigation of why compressibility reduces turbulent production is the next step. In the case of the shear layer, Vreman *et al.* (1996) showed that the reduction in turbulent production is due to reduced pressure fluctuations via the reduction in the pressure–strain term. A pressure–strain model based on deterministic vortex structures and associated pressure extrema was also proposed. In the case of uniform shear flow, Sarkar (1996) noted reduced pressure fluctuations in cases with high gradient Mach number and stated that a change in the pressure gradient term in the momentum equations (and the pressure–strain term in the Reynolds stress equations) leads to reduced levels of turbulence. Freund, Lele & Moin (2000) confirmed the reduction in the pressure–strain term in the annular mixing layer. The transverse correlation length scale was found to decrease with increased Mach number. It was further found that the reduction in pressure variance could be parameterized with either a transverse turbulence Mach number or the gradient Mach number.

In high-speed flows, disturbances have a limited region of upstream and cross-stream influence due to the finite speed of sound. It has been conjectured, for example Morkovin (1987), that this phenomenon of reduced communication is responsible for the reduced growth rates of instability modes in compressible shear flows. The idea of reduced cross-stream communication is relevant to the sonic-eddy model of Breidenthal (1990) as well as the reduced pressure extrema in the coherent-vortex model of Vreman *et al.* (1996). Papamoschou & Lele (1993), in a two-dimensional, inviscid, temporal simulation, obtained the evolution of fluctuations associated with an Oseen vortex embedded in a hyperbolic-tangent velocity profile. At high Mach

number, the pressure disturbance field was found to have reduced streamwise extent; however, unlike the assumption of the models, its extent in the cross-stream direction relative to the width of the shear layer was not noticeably affected. Evidently, the idea of reduced communication requires further investigation as does a mathematical framework for its link to the observed compressibility effects in turbulent shear flows.

Controversy exists on the effect of compressibility on the components of the Reynolds stress tensor,  $R_{ij}$ , and associated anisotropy. Laboratory data of Samimy & Elliot (1990), Barre, Quine & Dussauge (1994), and more recently, Chambres, Barre & Bonnet (1998) show that all measured turbulence intensities and the Reynolds shear stress decrease with increasing  $M_c$  leaving the Reynolds stress anisotropy relatively unchanged. However, Goebel & Dutton (1991) find experimentally that the streamwise component,  $R_{11}$ , changes little compared to the decrease in  $R_{22}$  and  $R_{12}$ , leading to large changes in the Reynolds stress anisotropy. It should be noted that experimental measurements of the spanwise turbulence intensity are available in only the studies of Chambres *et al.* (1998) and Gruber, Messersmith & Dutton (1993). The DNS study of the plane shear layer by Vreman *et al.* (1996) concludes that, although the normal stress anisotropies increase with  $M_c$ , the shear stress anisotropy remains relatively unaffected. Freund *et al.* (2000) in their DNS of the annular jet find that the normal stress anisotropies increase while the shear stress anisotropy decreases. DNS studies of uniformly sheared flow by Sarkar (1995) and Simone *et al.* (1997) show increased normal stress anisotropies as well as reduced shear stress anisotropy.

From the preceding discussion, it is clear that DNS studies have proved valuable in complementing experimental observations in attempts to understand the compressibility effect in turbulent shear flows. Conclusions from DNS databases are strengthened if the data are validated against available experimental results with fully developed turbulence. Direct validation of our DNS results with experimental profiles of turbulence intensity is an important objective of the present work.

In summary, although significant progress has been made in our understanding of the compressible shear layer, there remain unresolved questions. The present work addresses the following open questions. Why does the pressure-strain term decrease with increasing Mach number? What is the effect of density ratio on shear layer growth in the high-speed regime? What is the effect of compressibility on the turbulence anisotropy?

## 2. Problem formulation

### 2.1. Governing equations

The unsteady, three-dimensional, compressible Navier–Stokes equations are solved for the temporally evolving shear layer. The energy equation is written as a pressure equation where viscosity, diffusion, thermal conductivity and the specific heat ratio are constants. The equation of state corresponding to an ideal gas is assumed. Introducing the scales  $\mathcal{L}_o$ ,  $\mathcal{Q}_o$ ,  $\rho_o$  and  $\mathcal{U}_o$ , new non-dimensional variables are obtained where all dimensional variables are represented with script fonts

$$t = \frac{t\mathcal{U}_o}{\mathcal{L}_o}, \quad x_i = \frac{x_i}{\mathcal{L}_o}, \quad u_i = \frac{u_i}{\mathcal{U}_o}, \quad \rho = \frac{\rho}{\rho_o}, \quad p = \frac{p}{\rho_o}$$

giving the following non-dimensional conservation equations:

$$\frac{\partial \rho}{\partial t} + \frac{\partial(\rho u_k)}{\partial x_k} = 0, \quad (2.1)$$

$$\frac{\partial(\rho u_i)}{\partial t} + \frac{\partial(\rho u_k u_i)}{\partial x_k} = -\frac{1}{\gamma M^2} \frac{\partial p}{\partial x_i} + \frac{\partial \sigma_{ik}}{\partial x_k}, \quad (2.2)$$

$$\frac{\partial p}{\partial t} + u_k \frac{\partial p}{\partial x_k} = -\gamma p \frac{\partial u_k}{\partial x_k} + \gamma \frac{\partial}{\partial x_k} \left( \frac{1}{RePr} \frac{\partial}{\partial x_k} \left( \frac{p}{\rho} \right) \right) + (\gamma - 1) \gamma M^2 \phi, \quad (2.3)$$

with

$$\sigma_{ij} = \frac{1}{Re} \left\{ \frac{\partial u_i}{\partial x_j} + \frac{\partial u_j}{\partial x_i} - \frac{2}{3} \frac{\partial u_k}{\partial x_k} \delta_{ij} \right\}, \quad (2.4)$$

$$\phi = \sigma_{ij} \frac{\partial u_i}{\partial x_j}, \quad (2.5)$$

where the dimensionless numbers are defined in the usual way,

$$Re = \frac{\rho_o \mathcal{U}_o \mathcal{L}_o}{\mu}, \quad Pr = \frac{\mu c_p}{\kappa}, \quad M = \frac{\mathcal{U}_o}{\sqrt{\gamma \rho_o / \rho_o}}.$$

Furthermore, the reference quantities are chosen such that  $\gamma M^2 = 1$  leading to  $\rho_o = \rho_o \mathcal{U}_o^2$ .

## 2.2. Numerical scheme

The transport equations are integrated using a sixth order of accuracy compact Padé scheme in space as described by Lele (1992). The time advancement is performed with a fourth order of accuracy low-storage Runge–Kutta scheme as described by Williamson (1980). Periodic boundary conditions in the  $x_1$ - and  $x_3$ -directions are used and ‘non-reflective’ boundary conditions as studied by Thompson (1987) are imposed in the  $x_2$ -direction. A uniform grid is used. In order to avoid spurious numerical instabilities generated by aliasing errors in the nonlinear convective terms, the flow variables are filtered using a compact filter described by equation C.2.4 of Lele (1992). Sufficient resolution is used and the filter coefficient chosen as discussed by Lele (1992) to significantly affect only the highest wavenumbers. The choice of the frequency at which the filter is applied as well as the validation of the simulations is discussed in Appendix A.

## 2.3. Initial conditions

The flow is initialized to a hyperbolic tangent profile for the mean streamwise velocity,  $\bar{u}_1(x_2)$ , while all other mean velocity components are set to zero. Thus,

$$\bar{u}_1(x_2) = \frac{\Delta u}{2} \tanh \left( -\frac{x_2}{2\delta_\theta(0)} \right), \quad \bar{u}_2 = 0, \quad \bar{u}_3 = 0. \quad (2.6)$$

The upper stream has a velocity,  $-\Delta u/2$ , and the lower stream has a velocity,  $\Delta u/2$ , as shown in figure 1. The mean pressure is set to a uniform value  $p_o$ . The density in the upper stream  $\rho_1$ , and that in the lower stream  $\rho_2$ , are specified. The convective Mach number introduced by Bogdanoff (1993) and further studied by Papamoschou & Roshko (1988) is defined in the case of two streams with the same specific heat ratio  $\gamma$ , by

$$M_c = \frac{\Delta u}{c_1 + c_2}, \quad (2.7)$$

where  $c_1$  and  $c_2$  are the speeds of sound of each stream. In addition to these mean values, broadband fluctuations are used to accelerate the transition to turbulence. This

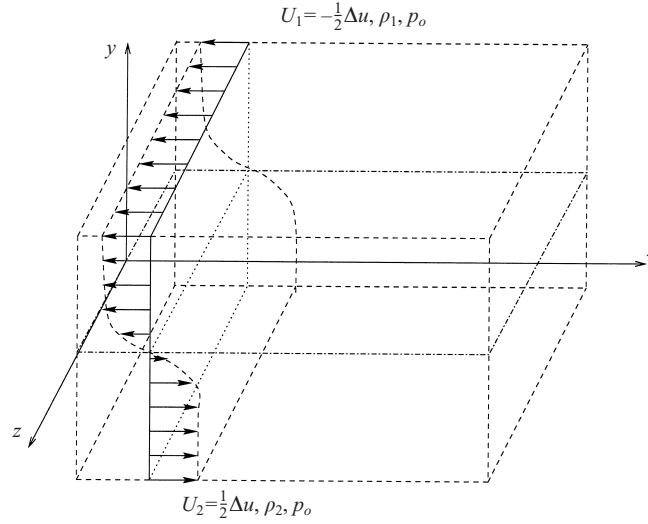


FIGURE 1. Schematic of the temporally evolving shear layer.

is achieved by generating a random field on which is imposed an isotropic turbulence spectrum of the form

$$E(k) = (k/k_o)^4 \exp(-2(k/k_o)^2), \quad (2.8)$$

where  $k$  is the wavenumber and  $k_o$  is the peak wavenumber. In the present simulations  $k_o$  is imposed so as to have 48 peak wavelengths within the streamwise direction for simulations A3 and A11 and half that value in the remaining cases. The initial turbulence intensity is set to 10%. The extent of the turbulence is limited in the cross-stream direction by an exponential decay over a thickness equal to the initial shear layer thickness. Solenoidality is imposed on this random turbulent field. Such quasi-incompressible fluctuations minimize compressibility transients as shown by Erlebacher *et al.* (1990). The pressure fluctuations are obtained from the Poisson equation for incompressible flow and the density from the isentropic equation of state.

#### 2.4. Simulation parameters

Two series of simulations are conducted. The parameters of series A are chosen to analyse the effects of  $M_c$  (compressibility) and those of series B to analyse the effect of variable density for a fixed  $M_c = 0.7$  case. The density ratio is defined as

$$s = \frac{\rho_2}{\rho_1}. \quad (2.9)$$

The average density,  $\rho_o = (\rho_1 + \rho_2)/2 = 1.0$ , is fixed in all the simulations. In series A, the mean density is uniform, while, in series B, the mean density profile is given by

$$\bar{\rho}(x_2) = \rho_o \left( 1 + \lambda(s) \tanh \left( -\frac{x_2}{2\delta_\theta(0)} \right) \right) \quad (2.10)$$

where

$$\lambda(s) = \frac{s-1}{s+1}. \quad (2.11)$$

The non-dimensional parameters in the governing equations are  $Re = 800$  and

Case	$M_c$	$s$	$L_x \times L_y \times L_z$	$N_x \times N_y \times N_z$
A3	0.3	1.0	$345 \times 172 \times 86$	$512 \times 256 \times 128$
A7	0.7	1.0	$172 \times 129 \times 86$	$256 \times 192 \times 128$
A11	1.1	1.0	$345 \times 172 \times 86$	$512 \times 256 \times 128$
B2	0.7	2.0	$172 \times 129 \times 86$	$256 \times 192 \times 128$
B4	0.7	4.0	$172 \times 129 \times 86$	$256 \times 192 \times 128$
B8	0.7	8.0	$172 \times 129 \times 86$	$256 \times 192 \times 128$

TABLE 1. Simulation parameters.  $L_x$ ,  $L_y$ , and  $L_z$  denote computational domain lengths measured in terms of initial momentum thickness while  $N_x$ ,  $N_y$ , and  $N_z$  denote the corresponding number of grid points.

Case	$Re_\omega$	$Re_\lambda$	$L_\eta/\Delta x$	$l_x/L_x$	$l_z/L_z$
A3	10026	134	0.34	0.049	0.065
A7	7790	114	0.33	0.095	0.041
A11	13640	120	0.38	0.030	0.028
B2	8590	115	0.33	0.099	0.025
B4	8330	126	0.30	0.178	0.051
B8	7404	128	0.26	0.126	0.036

TABLE 2. Final values of some non-dimensional parameters.  $L_\eta$  denotes the Kolmogorov scale, while  $l_x$  and  $l_z$  are the integral lengths in the streamwise and spanwise directions, respectively, associated with the the streamwise velocity.

$Pr = 0.7$  while  $\gamma = 1.4$ . The computational domain is given in table 1, where the physical domain is measured in terms of the initial shear layer momentum thickness  $\delta_\theta(0)$ . Such large domains are required to allow evolution to the self-similar state. The initial momentum thickness Reynolds number is  $Re_\theta = 160$  while the Reynolds number based on vorticity thickness has an initial value of  $Re_\omega = 640$ .

Table 2 gives final values of key non-dimensional parameters. The Reynolds numbers are large enough for turbulent flow. The integral length scales,  $l_x$  and  $l_z$ , are sufficiently small compared to the dimensions of the computational box to have good large-scale resolution and the grid size is sufficiently small to resolve the small scales. In our case the integral scales are given by

$$l_x = \frac{1}{u_1^2} \int_0^{L_x/2} \overline{u_1(\mathbf{x})u_1(\mathbf{x} + \mathbf{e}_1 r)} dr, \quad (2.12)$$

$$l_z = \frac{1}{u_1^2} \int_0^{L_z/2} \overline{u_1(\mathbf{x})u_1(\mathbf{x} + \mathbf{e}_3 r)} dr, \quad (2.13)$$

where  $\mathbf{e}_i$  is the unitary vector in the  $i$ -direction. The microscale Reynolds number evaluated at the centreline is defined as

$$Re_\lambda = q^2 \sqrt{\frac{5}{\nu \epsilon}}, \quad (2.14)$$

where  $q^2$  is twice the turbulent kinetic energy.

It is important to validate the numerics. Sections A.1–A.3 of the Appendix describe the following validation issues with respect to our DNS: accuracy of large-scale representation in a finite domain, accuracy of small-scale representation by the

chosen grid cell size, and the impact of the numerical filter on the results. The overall conclusion is that the simulations are well-resolved.

### 3. Characteristics of the shear layer

The approach of the turbulent shear layer towards a state where the mean and r.m.s. velocity profiles evolve self-similarly, after an initial transient, has been observed in many studies. Experimental studies of the evolution to self-similarity of the incompressible case include those by Bell & Mehta (1990) and Spencer & Jones (1971), which are used to validate the current DNS. Among the previous DNS studies of the incompressible shear layer, that by Rogers & Moser (1994) contains a detailed analysis of the turbulent kinetic energy budget in the self-similar shear layer and was therefore also chosen to validate our low-Mach-number case (their simulation labelled TBL was used for comparison). Experimental results on the compressible shear layer have been obtained by Papamoschou & Roshko (1988), Elliot & Samimy (1990), Barre *et al.* (1994), Chambers *et al.* (1998) and DNS results obtained by Vreman *et al.* (1996), Freund *et al.* (2000) among others. These results are compared with the high-Mach-number simulations performed here.

Exact self-similarity is more difficult to achieve in DNS than in experiments because of the finite domain size achievable with current computational resources. Nevertheless, it is instructive to plot profiles using self-similar coordinates so as to quantify the approach to self-similarity, and compare with experimental data.

#### 3.1. Favre-averaged equations

It is customary to use Favre averaging to express the mean mass and momentum conservation equations for compressible flows. By definition, the Favre average of a variable  $\phi$  is

$$\tilde{\phi} = \frac{\overline{\rho\phi}}{\bar{\rho}} \quad (3.1)$$

where  $\bar{\phi}$  denotes the Reynolds average that, in our case, is obtained by plane averaging along the periodic  $x_1, x_3$ -directions. Note that  $\phi'$  denotes Reynolds fluctuations and  $\phi''$  denotes Favre fluctuations. The turbulent stress tensor  $R_{ij}$  is defined by

$$R_{ij} = \frac{\overline{\rho u_i'' u_j''}}{\bar{\rho}}. \quad (3.2)$$

Using these definitions, the following system of equations is obtained:

$$\frac{\partial \bar{\rho}}{\partial t} + \frac{\partial(\bar{\rho} \tilde{u}_k)}{\partial x_k} = 0, \quad (3.3)$$

$$\frac{\partial(\bar{\rho} \tilde{u}_i)}{\partial t} + \frac{\partial(\bar{\rho} \tilde{u}_k \tilde{u}_i)}{\partial x_k} = -\frac{\partial \bar{p}}{\partial x_i} + \frac{\partial}{\partial x_k} (\bar{\sigma}_{ik} - \bar{\rho} R_{ik}), \quad (3.4)$$

$$\frac{\partial \bar{p}}{\partial t} + \tilde{u}_k \frac{\partial \bar{p}}{\partial x_k} = -(\gamma - 1)(\Pi - \bar{\phi}) - \gamma \bar{p} \frac{\partial \tilde{u}_k}{\partial x_k} - \frac{\partial}{\partial x_k} \left( \overline{p' u_k'} - \frac{\gamma \kappa^*}{RePr} \frac{\partial T}{\partial x_k} \right). \quad (3.5)$$

In the mean energy equation (3.5),  $\Pi = \overline{p'd'}$  represents the pressure–dilatation correlation with  $d'$  denoting the fluctuating component of dilatation,  $\nabla \cdot \mathbf{u}$ . The Reynolds

stress transport equation is given by

$$\frac{\partial(\bar{\rho}R_{ij})}{\partial t} + \frac{\partial(\bar{\rho}\tilde{u}_k R_{ij})}{\partial x_k} = \bar{\rho}(P_{ij} - \epsilon_{ij}) - \frac{\partial T_{ijk}}{\partial x_k} + \Pi_{ij} + \Sigma_{ij}, \quad (3.6)$$

where the turbulent production, dissipation, transport, pressure–strain and mass flux coupling terms are, respectively

$$\begin{aligned} P_{ij} &= - \left( R_{ik} \frac{\partial \tilde{u}_j}{\partial x_k} + R_{jk} \frac{\partial \tilde{u}_i}{\partial x_k} \right), \\ \epsilon_{ij} &= \frac{1}{\bar{\rho}} \left( \overline{\tau'_{jk} \frac{\partial u''_i}{\partial x_k}} + \overline{\tau'_{ik} \frac{\partial u''_j}{\partial x_k}} \right), \\ T_{ijk} &= \overline{\rho u''_i u''_j u''_k} + \overline{p' u''_i \delta_{jk}} + \overline{p' u''_j \delta_{ik}} - (\overline{\tau'_{jk} u''_i} + \overline{\tau'_{ik} u''_j}), \\ \Pi_{ij} &= \overline{p' \left( \frac{\partial u''_i}{\partial x_j} + \frac{\partial u''_j}{\partial x_i} \right)}, \\ \Sigma_{ij} &= \overline{u''_i} \left( \frac{\partial \bar{\tau}_{jk}}{\partial x_k} - \frac{\partial \bar{p}}{\partial x_j} \right) + \overline{u''_j} \left( \frac{\partial \bar{\tau}_{ik}}{\partial x_k} - \frac{\partial \bar{p}}{\partial x_i} \right). \end{aligned}$$

The following transport equation for the turbulent kinetic energy,  $K = R_{kk}/2$ , is obtained from (3.6) by contracting the indices:

$$\frac{\partial(\bar{\rho}K)}{\partial t} + \frac{\partial(\bar{\rho}\tilde{u}_k K)}{\partial x_k} = \bar{\rho}(P - \epsilon) - \frac{\partial T_k}{\partial x_k} + \overline{p' \frac{\partial u''_k}{\partial x_k}} + \Sigma_{kk}/2. \quad (3.7)$$

All averaged quantities are functions of time  $t$  and the transverse coordinate  $x_2$  only, allowing some simplifications to be introduced later.

### 3.2. Self-similar equations

In order to obtain a set of equations representing the self-similar state, a measure of the shear layer thickness is introduced. The momentum thickness,  $\delta_\theta$ , is defined by

$$\delta_\theta(t) = \frac{1}{\rho_o \Delta u^2} \int_{-\infty}^{\infty} \bar{\rho} \left( \frac{1}{2} \Delta u - \tilde{u}_1 \right) \left( \frac{1}{2} \Delta u + \tilde{u}_1 \right) dx_2. \quad (3.8)$$

After differentiating (3.8) with respect to time and using the averaged momentum equation, the following expression for the non-dimensional growth rate of the momentum thickness is obtained, as shown by Vreman *et al.* (1996):

$$\dot{\delta}_\theta = \frac{1}{\Delta u} \frac{d\delta_\theta}{dt} = \frac{2}{\rho_o \Delta u^3} \int_{-\infty}^{\infty} (\bar{\sigma}_{12} - \bar{\rho} R_{12}) \frac{\partial \tilde{u}_1}{\partial x_2} dx_2. \quad (3.9)$$

The mean viscous effects can be neglected for developed shear layers, see (3.18), and consequently, the shear layer growth rate can be expressed as

$$\dot{\delta}_\theta = - \frac{2}{\rho_o \Delta u^3} \int_{-\infty}^{\infty} \bar{\rho} R_{12} \frac{\partial \tilde{u}_1}{\partial x_2} dx_2. \quad (3.10)$$

At this point the self-similar coordinate  $\eta$ , defined by  $\eta = x_2/\delta_\theta(t)$ , can be introduced and derivatives with respect to  $x_2$  and  $t$  can be calculated. Introduction of new self-similar functions along with the self-similar coordinate requires paying special attention to the order of magnitude of the different terms in the respective conservation equations. A specified dependence on velocity difference, mean density and growth

rate is chosen for the assumed functions; this dependence will be validated against DNS results in the analysis. All functions depend on the convective Mach number  $M_c$  and  $s$ , the density ratio; for example,  $\hat{\rho}(\eta)$  in (3.11) below denotes  $\hat{\rho}(\eta; M_c, s)$ . However, for simplicity, this dependence is not shown explicitly. Thus,

$$\bar{\rho} = \rho_o \hat{\rho}(\eta), \quad (3.11)$$

$$\tilde{u}_1 = \Delta u \hat{u}_1(\eta), \quad (3.12)$$

$$\tilde{u}_2 = \Delta u (\dot{\delta}_\theta)^n \hat{u}_2(\eta), \quad (3.13)$$

$$R_{12} = \Delta u^2 (\dot{\delta}_\theta)^m \hat{R}_{12}(\eta). \quad (3.14)$$

It has been assumed that  $\tilde{u}_2$  and  $R_{12}$  depend on the non-dimensional temporal growth rate of the momentum thickness  $\dot{\delta}_\theta$ . The governing equations suggest such a dependence, as will become clear shortly. Introducing the functions defined in (3.11)–(3.13) into the mass conservation equation, (3.3), gives

$$-\eta \frac{d\hat{\rho}(\eta)}{d\eta} + \frac{d}{d\eta} (\hat{\rho}(\eta) \hat{u}_2(\eta) (\dot{\delta}_\theta)^{n-1}) = 0. \quad (3.15)$$

The choice  $n = 1$ , makes (3.15) independent of the growth rate, giving the self-similar equation

$$-\eta \frac{d\hat{\rho}(\eta)}{d\eta} + \frac{d}{d\eta} (\hat{\rho}(\eta) \hat{u}_2(\eta)) = 0. \quad (3.16)$$

Similarly, the streamwise momentum equation is transformed to

$$-\eta \frac{d}{d\eta} (\hat{\rho}(\eta) \hat{u}_1(\eta)) + \frac{d}{d\eta} (\hat{\rho}(\eta) \hat{u}_2(\eta) \hat{u}_1(\eta)) = -\frac{d}{d\eta} (\hat{\rho}(\eta) \hat{R}_{12}(\eta) (\dot{\delta}_\theta)^{m-1}) + \frac{d}{d\eta} \left( \frac{1}{Re \rho_o \Delta u \dot{\delta}_\theta} \frac{d}{d\eta} (\bar{u}_1 / \Delta u) \right). \quad (3.17)$$

For a turbulent shear layer, it is clear that the Reynolds stress  $R_{12}$  must be of the same order as the convective terms, giving  $m = 1$ . The Reynolds number based on the momentum thickness can be defined as  $Re_\theta = \rho_o Re \Delta u \dot{\delta}_\theta$ .

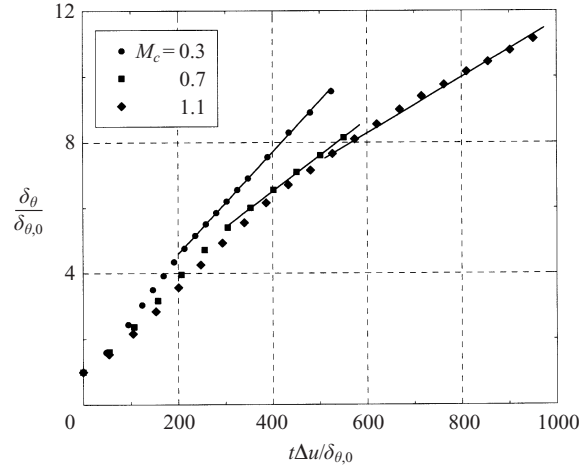
An order of magnitude estimate of the mean viscous terms can be now obtained. The mean velocity derivative in the last term of (3.17) can be estimated using  $d\bar{u}_1/dx_2 \simeq \Delta u / \delta_\omega$ , where the vorticity thickness is  $\delta_\omega = \Delta u / (\partial \bar{u}_1 / \partial x_2)_{max}$ . The vorticity thickness can be related to the momentum thickness by  $\delta_\omega = D_\omega \dot{\delta}_\theta$ . The value of  $D_\omega$  for the turbulent mixing layer is dependent on  $M_c$  and  $s$ , and can be calculated from the DNS database, giving a nominal value of  $D_\omega \approx 5.0$  in the low-speed case. From the DNS results it is observed that  $D_\omega$  increases with  $M_c$ . Since the self-similar region of the turbulent shear layer requires that the viscous term, which has a dependence on  $\dot{\delta}_\theta$ , be negligible in comparison with the Reynolds stress term, the following condition is required:

$$D_\omega Re_\theta \dot{\delta}_\theta \gg 1, \quad (3.18)$$

giving the simplified self-similar momentum equation

$$(\hat{u}_2(\eta) - \eta) \hat{\rho}(\eta) \frac{d\hat{u}_1(\eta)}{d\eta} = -\frac{d}{d\eta} (\hat{\rho}(\eta) \hat{R}_{12}(\eta)). \quad (3.19)$$

In summary, (3.16) and (3.19) are the self-similar forms of the mean mass and momentum conservation equations, respectively.

FIGURE 2. Momentum thickness evolution with time for different  $M_c$ .

### 3.3. The baseline incompressible shear layer

The purpose of this section is to validate our computational model by comparing our results with experimental and DNS data obtained by other researchers. Unfortunately, experimental data are limited in most cases to mean and r.m.s. velocity measurements. It would be of great interest to compare experimental values of all the terms in the turbulent kinetic energy budget. Accurate measurements of all these terms are rare in the literature, mainly due to intrinsic difficulties in measurements of turbulent dissipation at high Reynolds numbers. Instead, the DNS results of Rogers & Moser (1994) are used for validating the balance of turbulent kinetic energy. Case A3 was chosen as reference for the incompressible comparisons since  $M_c = 0.3$  is sufficiently small for compressibility effects to be considered negligible. It will be seen in the next section that this case is, for all purposes, quasi-incompressible.

It is generally accepted that, after an initial transient, the shear layer grows linearly. Figure 2 shows the momentum thickness evolution for simulations A3, A7 and A11. For comparison, a linear regression is also plotted. It can be observed that approximate linear growth is achieved. The normalized time is defined as

$$\tau = \frac{t\Delta u}{\delta_\theta(0)}.$$

The growth rate for the quasi-incompressible case is calculated from the DNS to be  $\dot{\delta}_\theta = 0.0184$ . The growth rate of a spatially evolving shear layer is often expressed as

$$\frac{d\delta_\omega}{dx} = C_\delta \frac{U_1 - U_2}{U_1 + U_2}, \quad (3.20)$$

where the constant  $C_\delta \simeq 0.16$ . The corresponding growth rate of a temporally evolving shear layer, assuming a convective velocity  $(U_1 + U_2)/2$ , is

$$\dot{\delta}_\theta = \frac{1}{\Delta u} \frac{d\delta_\theta}{dt} = \frac{1}{D_\omega \Delta u} \frac{d\delta_\omega}{dt} = \frac{C_\delta}{2D_\omega} \simeq 0.016, \quad (3.21)$$

with which the DNS result is in good agreement. The condition in (3.18) is also calculated in order to evaluate the importance of the mean viscous term, and it is found that  $D_\omega Re_\theta \dot{\delta}_\theta > 80$  during the late-time evolution,  $\tau > 261$ . Figures 3(a) and 3(b) show the evolution of the streamwise turbulent intensity and the normalized

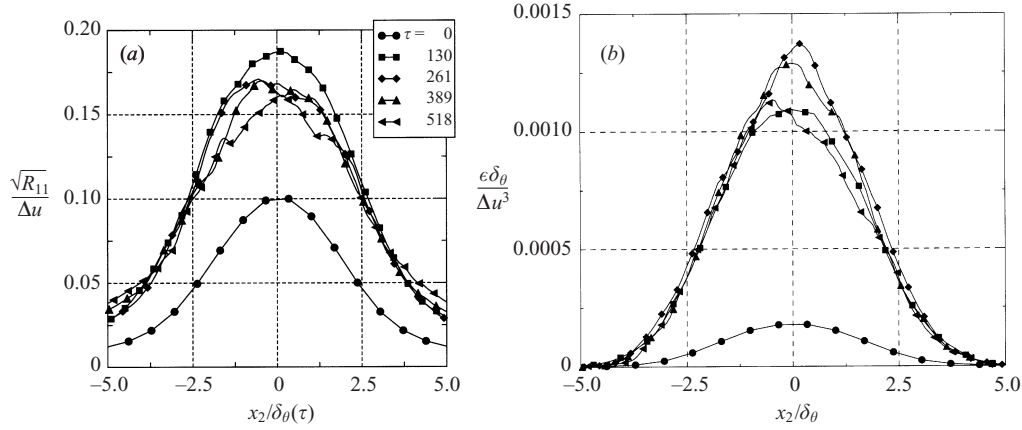


FIGURE 3. Time evolution of (a) streamwise velocity fluctuation r.m.s., and (b) normalized turbulent dissipation rate  $M_c = 0.3$ .

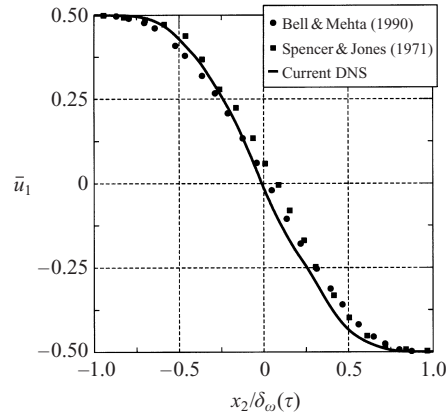


FIGURE 4. Mean streamwise velocity.

dissipation as a function of time. Both quantities increase from a low initial value during a transient period, reach a maximum, and eventually decay to their self-similar values. Beyond  $\tau = 261$ , the variation in the profiles is smaller, showing an approach towards self-similarity.

The DNS results are compared with experimental results obtained by Bell & Mehta (1990) and Spencer & Jones (1971) for incompressible shear layers. In order to perform the comparisons, an ensemble average is extracted from the profiles plotted in self-similar coordinates. This average is obtained from profiles in the time interval,  $261 < \tau < 518$ . Figure 4 compares different experimental measurements with the ensemble average of the DNS profiles of the streamwise velocity. Good agreement is obtained. Cross-stream profiles of velocity intensities are compared against experiments in figures 5(a), 5(b) and 5(c). The peak turbulence intensities in the DNS are: streamwise,  $\sqrt{R_{11}}/\Delta u = 0.17$ , transverse,  $\sqrt{R_{22}}/\Delta u = 0.134$ , and spanwise,  $\sqrt{R_{33}}/\Delta u = 0.145$ . The peak intensities and the self-similar shape agree well with both experiments and the previous DNS by Rogers & Moser (1994). It can be seen that the fluctuations are strongly three-dimensional with streamwise  $>$  spanwise  $>$  transverse intensity. Present results on the turbulence profiles differ little from

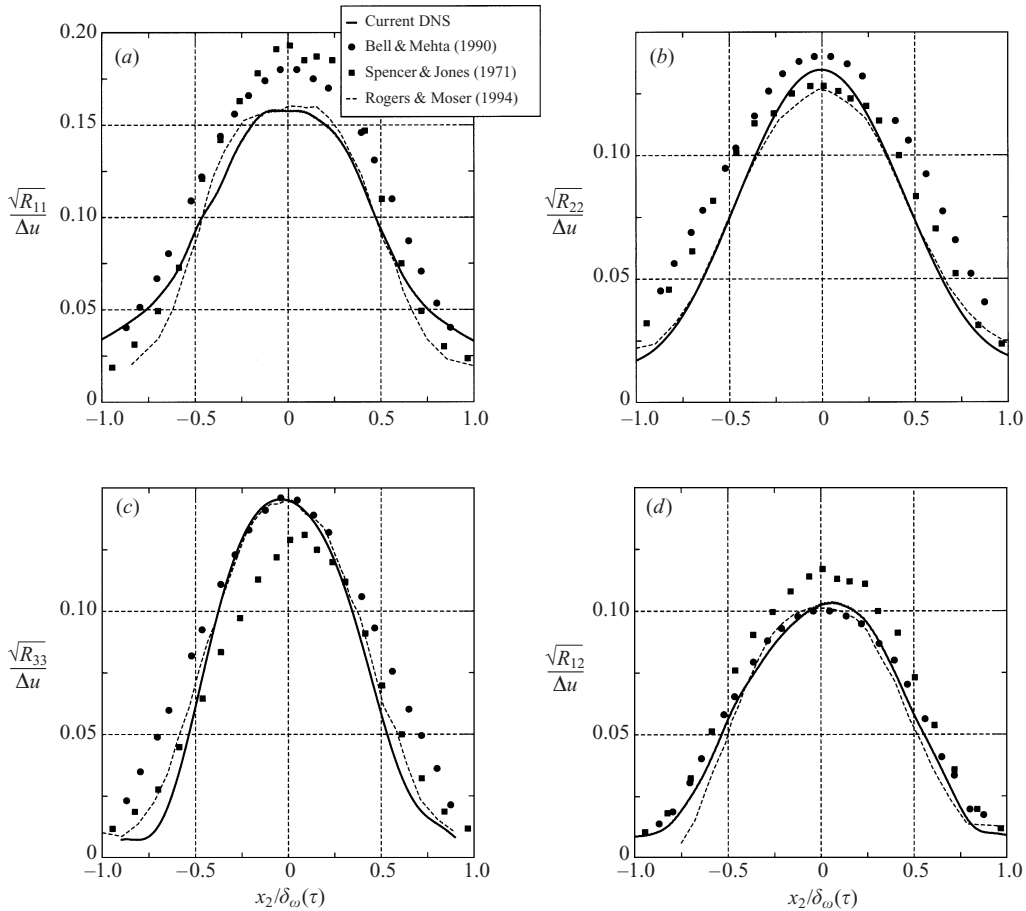


FIGURE 5. (a) Streamwise (b) vertical and (c) spanwise r.m.s. velocity; and (d) Reynolds shear stress. DNS at  $M_c = 0.3$ .

those reported by Rogers & Moser (1994), where a different type of broadband initial fluctuations was used. Those simulations were initialized with imposed fluctuations from boundary layer turbulence obtained from previous DNS, while the current DNS has quasi-random initial fluctuations. It should be noted that self-similar turbulence profiles were achieved by  $\tau = 100$  in the simulations of Rogers & Moser (1994). Figure 5(d) shows the normalized square root of the Reynolds shear stress. Its maximum value is 0.103, which gives

$$\frac{R_{12}}{\Delta u^2 \delta_\theta} \simeq 0.58, \quad (3.22)$$

suggesting that the initial assumption of  $\Delta u^2 \delta_\theta$  for normalizing the Reynolds stress to obtain  $O(1)$  quantities is correct. Comparisons of production, dissipation and transport in the temporal kinetic energy budget are shown compared to the results of Rogers & Moser (1994) in figure 6. Note that the production, dissipation and transport correspond to the first, second and third terms respectively, on the right-hand side of (3.7); the fourth and fifth terms are always negligible in the cases studied ( $M_c \leq 1.1$ ). In our present simulations the level of production and transport are somewhat larger (approximately 10%) than the values observed by Rogers & Moser

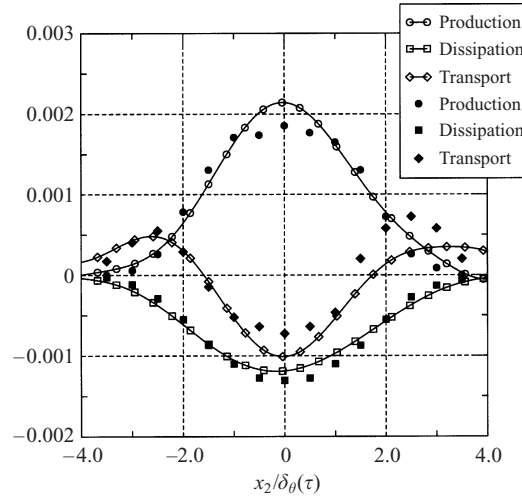


FIGURE 6. Turbulent kinetic energy budget: production, transport and dissipation. The budget terms are normalized by  $\Delta U^3/\delta_\theta$ . Symbols: DNS results of Rogers & Moser (1994), lines: current DNS at  $M_c = 0.3$ .

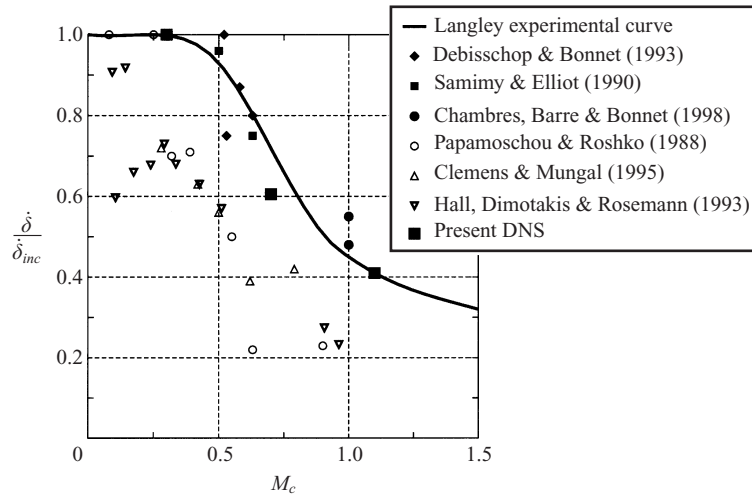
(1994). On the other hand, the turbulent dissipation profile agrees very well, showing that the simulation is correctly resolved.

In summary, the baseline, quasi-incompressible case with  $M_c = 0.3$  has been successfully validated against previous studies of the incompressible shear layer. Profiles of turbulence intensities which agree well with both experiments and DNS are obtained in our simulations. The balance of turbulent kinetic energy in the self-similar state obtained from the current DNS shows remarkably good agreement with the previous DNS of Rogers & Moser (1994) even though the initial broadband fluctuations in the two simulations have very different characteristics.

### 3.4. The compressible shear layer

The shear layer momentum thickness evolution with time is plotted in figure 2 for the cases A3, A7 and A11. As can be seen, linear growth rates are achieved in all cases after an initial transient. The time required to reach this linear growth state is dependent on the convective Mach number, since all other parameters in the simulations were kept constant. Shear layer thickness growth rate from different experiments is plotted along with current DNS results in figure 7. The large reduction in growth rate that is seen in experiments is also seen in the current DNS. These DNS results closely match the so-called ‘Langley Experimental Curve’, obtained from a compilation of results corresponding to experiments with air–air shear layers. Differences with the results of Papamoschou & Roshko (1988) could be due to density ratio effects.

One of the differences observed in the DNS regarding the evolution of the compressible shear layer with respect to its incompressible counterpart is that the time required to achieve approximate self-similarity increases with compressibility. A possible explanation can partially be found in (3.18). The large reduction in the shear layer growth rate with compressibility is accepted and recognized as a fundamental feature of this kind of flow. Since the left-hand side of the self-similarity condition, (3.18), decreases when the shear layer thickness and thickness growth rate decrease, it is reasonable to deduce that it will require a longer time to achieve self-similarity with increasing  $M_c$ . A similar effect was observed by Elliot & Samimy (1990) in their experiments, who reported that a longer distance from the splitter plate tip was

FIGURE 7. Dependence of shear layer growth rate on  $M_c$ .

needed to achieve self-similarity for larger convective Mach numbers. Comparison with the result for  $M_c = 0.3$  shows that the  $M_c = 1.1$  case becomes approximately self-similar at  $\tau \approx 500$  compared to  $\tau \approx 300$  required for the  $M_c = 0.3$  case.

Figure 8(a) shows production, dissipation and transport for the A series. It can be clearly seen that production is much more affected by compressibility than dissipation. The current DNS agrees with the previous DNS of the mixing layer by Vreman *et al.* (1996) and Freund *et al.* (2000) that show decreased turbulence production with increasing  $M_c$ . Figure 8(b) shows the split of the transport term into its components. The turbulent transport is generally larger in magnitude than the pressure transport. The viscous transport is not shown since it is negligible relative to the other two components. Appendix C shows the budgets for various components of the Reynolds stress tensor,  $R_{ij}$ . The overall conclusion is that production, pressure-strain and transport terms are significantly reduced at high  $M_c$  while the dissipation changes relatively little.

The dependence of the peak velocity intensities on  $M_c$  is shown in figures 9(a) and 9(b). All components including that in the spanwise direction ( $\sqrt{R_{33}}/\Delta U = 0.14, 0.12, 0.11$  for  $M_c = 0.3, 0.7$  and  $1.1$ , respectively) decrease with increasing Mach number in the current DNS. The dependence of Reynolds stresses on  $M_c$  will be discussed further in § 5. Comparison of the turbulence profiles with experimental measurements by Elliot & Samimy (1990) at  $M_c = 0.64$  and present DNS results at  $M_c = 0.7$  are shown in figures 10(a), 10(b) and 10(c). The agreement with the experiments is excellent.

#### 4. Analysis of the compressibility effect of reduced growth rate

In the previous section, it was shown that the normalized turbulent production term,  $P$ , decreases with increasing convective Mach number in the simulations. The decreased level of production is responsible for the reduction of the vorticity thickness growth rate and turbulent kinetic energy of the shear layer, in agreement with the conclusion drawn by Sarkar (1995) from DNS of uniformly sheared flow. In the case of the momentum thickness of the mixing layer, the compressibility effect of decreased growth rate must be associated with a reduced level of normalized,

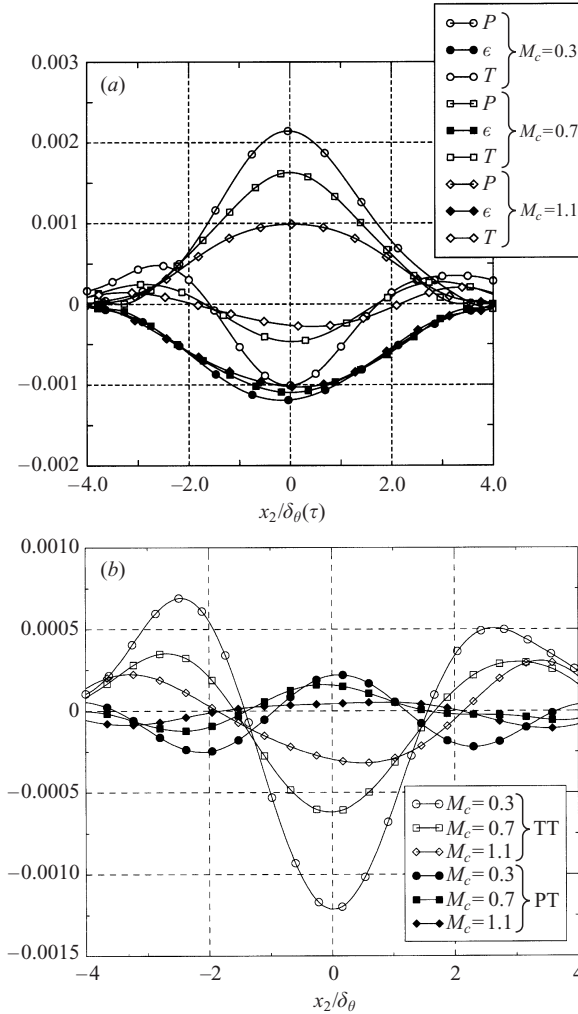


FIGURE 8. (a) Turbulent production, turbulent dissipation and the transport term, each normalized by  $\Delta U^3/\delta_\theta$ , for different  $M_c$ . The pressure dilatation and compressible dissipation are small and not shown. (b) Split of the transport term into turbulent transport (TT) and pressure transport (PT). The viscous transport is negligibly small and is not shown.

integrated turbulent production according to (3.10) as first shown by Vreman *et al.* (1996).

Section 4.1 confirms the earlier DNS observations of Vreman *et al.* (1996), Sarkar (1996) and Freund *et al.* (2000) regarding the change of pressure–strain with compressibility and, following the development of Vreman *et al.* (1996), links the pressure–strain term to the growth rate reduction. Section 4.2 is a new analysis that explains why the pressure–strain term decreases with increasing Mach number in turbulent shear flows. Furthermore, the analysis is used to develop a statistical model for the pressure–strain term.

#### 4.1. The Reynolds stress balance at high speeds

The transport equation for  $R_{11}$  is obtained from (3.6) and is

$$\frac{\partial(\bar{\rho}R_{11})}{\partial t} + \frac{\partial(\bar{\rho}\tilde{u}_2R_{11})}{\partial x_2} = \bar{\rho}(P_{11} - \epsilon_{11}) - \frac{\partial T_{112}}{\partial x_2} + \Pi_{11}. \quad (4.1)$$

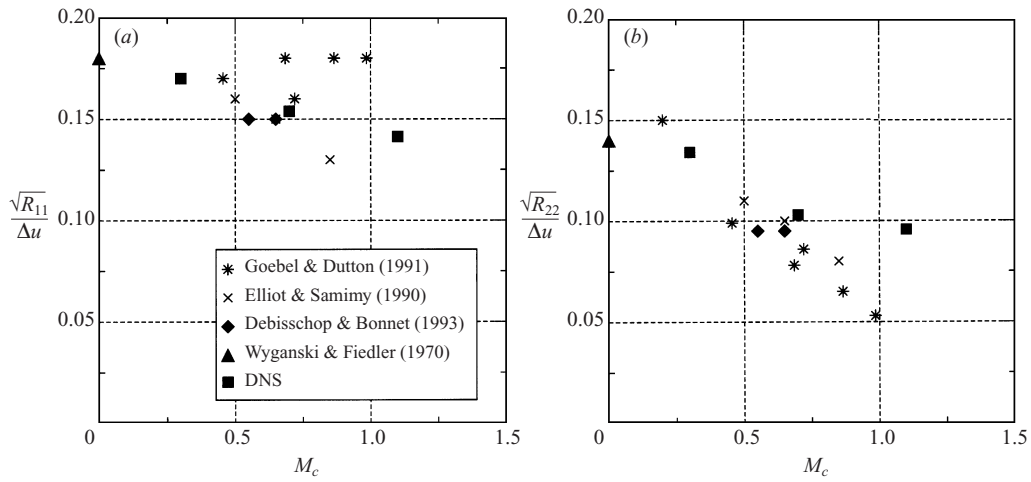


FIGURE 9. Dependence of peak (a) streamwise and (b) transverse r.m.s. velocity on  $M_c$ .

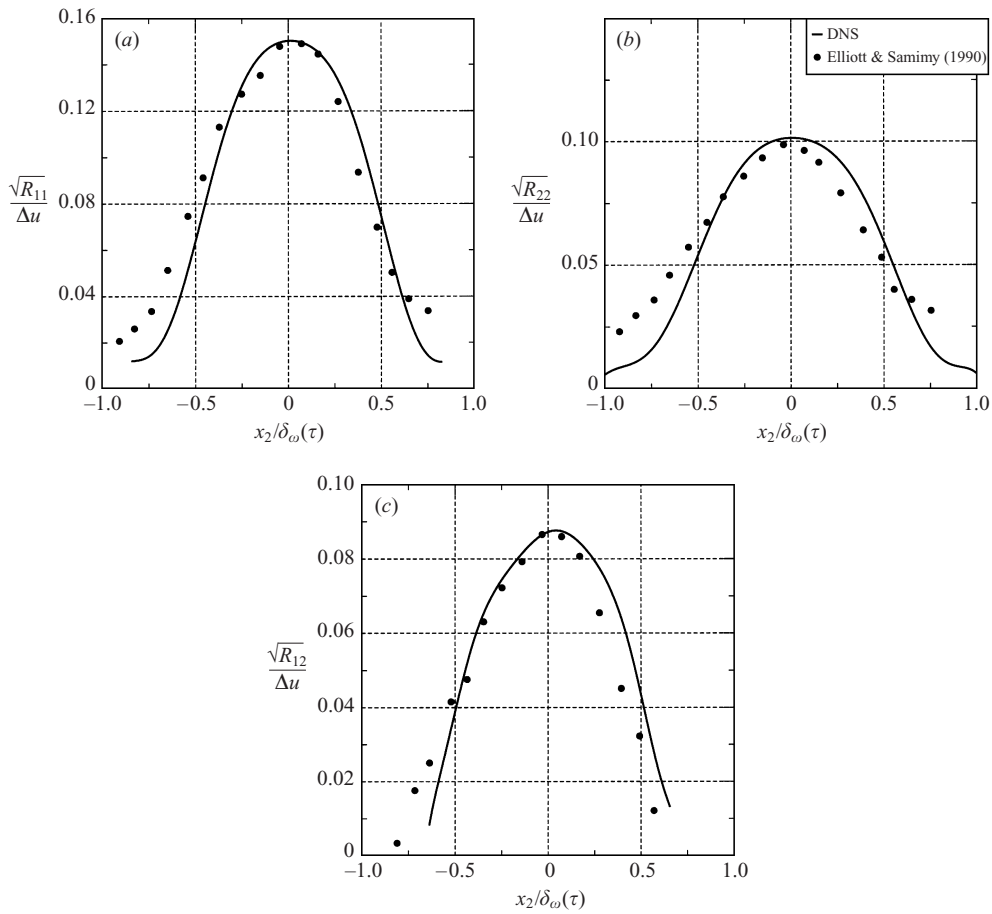


FIGURE 10. (a) Streamwise and (b) cross-stream r.m.s. velocity, and (c) Reynolds shear stress in compressible shear layer. DNS at  $M_c = 0.7$ , symbols correspond to experimental data at  $M_c = 0.64$ .

$M_c$	$\dot{\delta}_\theta$	$\bar{\epsilon}_{11} - \bar{\Pi}_{11}$	$\bar{R}_{11}$	$z$	$Q(z)$	Error	$\bar{\epsilon}_{11}$
0.3	0.0184	$1.568 \times 10^{-2}$	8.080	$1.267 \times 10^{-1}$	1.168	$-1.7 \times 10^{-5}$	$3.8 \times 10^{-3}$
0.7	0.0108	$9.711 \times 10^{-3}$	9.619	$9.341 \times 10^{-2}$	1.114	$-3.3 \times 10^{-5}$	$3.17 \times 10^{-3}$
1.1	0.0078	$7.125 \times 10^{-3}$	11.226	$7.999 \times 10^{-2}$	1.095	$-8.8 \times 10^{-6}$	$3.03 \times 10^{-3}$

TABLE 3. Variation of terms in (4.3) and (4.5) with  $M_c$ .

Here, the mass flux coupling term  $\Sigma_{11}$  has been neglected since, even in the large- $M_c$  case, its magnitude is negligible. Non-dimensionalizing the dissipation term by  $\Delta u^3/\delta_\theta$ , the pressure-strain and transport terms by  $\rho_o \Delta u^3/\delta_\theta$  on the right-hand side of the Reynolds stress transport equation and the Reynolds stress by  $\Delta u^2 \delta_\theta$ , and denoting the non-dimensional functions by a caret, gives the self-similar equivalent of (4.1). The only minor difference with the earlier work of Vreman *et al.* (1996) is the absorption of a  $\dot{\delta}_\theta$  term in the definition of  $\hat{R}_{11}$ . After integrating across the self-similar coordinate, the following equation is obtained:

$$(\dot{\delta}_\theta)^2 \int_{-\infty}^{\infty} \hat{\rho}(\eta) \hat{R}_{11}(\eta) d\eta = \dot{\delta}_\theta - \int_{-\infty}^{\infty} \hat{\rho}(\eta) \hat{\epsilon}_{11}(\eta) d\eta + \int_{-\infty}^{\infty} \hat{\Pi}_{11}(\eta) d\eta. \quad (4.2)$$

Introducing the overbar to denote the density-weighted integrals in the above equation, the following equation for the growth rate,  $\dot{\delta}_\theta$ , is obtained:

$$\dot{\delta}_\theta - (\dot{\delta}_\theta)^2 \bar{R}_{11} = \bar{\epsilon}_{11} - \bar{\Pi}_{11} \quad (4.3)$$

whose solution is

$$\dot{\delta}_\theta = \frac{1 - \sqrt{1 - 4\bar{R}_{11}(\bar{\epsilon}_{11} - \bar{\Pi}_{11})}}{2\bar{R}_{11}}. \quad (4.4)$$

Equation (4.4) for  $\dot{\delta}_\theta$  has only minor differences with respect to expressions obtained from the transport equation for  $R_{11}$  by Vreman *et al.* (1996) and Freund *et al.* (2000). Defining  $z = \bar{R}_{11}(\bar{\epsilon}_{11} - \bar{\Pi}_{11})$ , (4.4) can be approximated (since  $z \ll 1$ ) by

$$\dot{\delta}_\theta = (\bar{\epsilon}_{11} - \bar{\Pi}_{11})Q(z), \quad (4.5)$$

where

$$Q(z) = 1 + z + 2z^2 + 5z^3 + O(z^4). \quad (4.6)$$

Equations directly relating the thickness growth rate and the pressure-strain term were derived by Vreman *et al.* (1996) and Freund *et al.* (2000); (4.5) is similar to these previous relationships.

Table 3 shows measured values of  $\dot{\delta}_\theta$ ,  $\bar{\epsilon}_{11} - \bar{\Pi}_{11}$  and  $\bar{R}_{11}$  from which  $z$  and  $Q(z)$  can be calculated. The last column reports the calculated error when the measured values of  $\dot{\delta}_\theta$ ,  $\bar{\epsilon}_{11} - \bar{\Pi}_{11}$  and  $\bar{R}_{11}$  are used in the self-similar equation, (4.3). We associate this small error to the approximate self-similar state of the flow. From the values shown in table 3, it can be seen that the term  $\bar{\epsilon}_{11} - \bar{\Pi}_{11}$  varies strongly with  $M_c$ , while  $Q(z)$  is only weakly affected. The convective Mach number,  $M_c$ , affects  $\bar{\epsilon}_{11} - \bar{\Pi}_{11}$  by reducing its magnitude (notice that  $\bar{\Pi}_{11}$  is negative) and, subsequently, the momentum thickness growth rate is reduced as a consequence of (4.5). From the DNS database it is seen that only  $\bar{\Pi}_{11}$  is strongly affected by  $M_c$ , suggesting that the effect of  $M_c$  on the pressure-strain term is responsible for the reduction of the shear layer growth rate. The pressure strain term can only be reduced if the intensities of  $p'$  or  $\partial u'_1/\partial x_1$  are reduced. From the DNS it is clear that the dominant reduction is in the r.m.s.

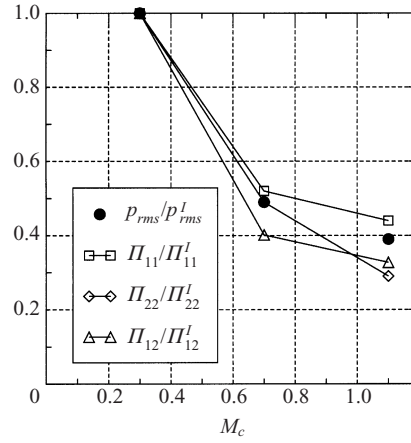


FIGURE 11. Open symbols  $\bar{\Pi}_{ij}/\bar{\Pi}_{ij}^I$  and filled symbols  $p_{rms}/p_{rms}^I$ . Each quantity is normalized by its incompressible counterpart.

pressure. Figure 11 shows that  $\bar{\Pi}_{11}$  and  $p_{rms}$ , normalized by their incompressible values, decrease similarly.

After confirming the results of previous investigations that the compressibility effects of reduced thickness growth rate and turbulence intensities are related to decreased pressure fluctuations, we now perform an analysis to explain the observed Mach number effects on the pressure–strain.

#### 4.2. The pressure–strain term at high speeds

In strictly incompressible flow, the instantaneous pressure has ‘infinite’ signal speed and satisfies a Poisson equation whose source is related to the velocity gradients. In the case of compressible flow, pressure fluctuations travel with the speed of sound,  $c_0$ . The consequence of a ‘finite’ signal speed on the pressure–strain term is now studied analytically.

The evolution equation for  $p'$ ,

$$\frac{1}{c_0^2} \frac{D^2 p'}{Dt^2} - \frac{\partial^2 p'}{\partial x_i \partial x_i} = \frac{\partial^2}{\partial x_i \partial x_j} (\rho u_i u_j)', \quad (4.7)$$

can be derived by taking the divergence of the momentum equation, and assuming that the isentropic relationship,  $Dp/Dt = c_0^2 D\rho/Dt$ , applies and viscous terms are negligible. Such assumptions are reasonable for high-Reynolds-number flows away from shocks and solid boundaries.

Equation (4.7) is now specialized to the centre of the shear layer where the mean velocity is zero and  $\partial \bar{u}_1/\partial x_2 = S \simeq \text{constant}$ . An analysis, assuming locally homogeneous turbulence in the physical domain located around the centre of the shear layer, is performed. The right-hand side of (4.7) that includes the mean shear as well as nonlinear terms is denoted by  $f'$ . In Fourier space, the following equation results:

$$\frac{\partial^2 \hat{p}}{\partial t^2} + c_0^2 k^2 \hat{p} = c_0^2 \hat{f}, \quad (4.8)$$

where  $\hat{p}$  and  $\hat{f}$  are the Fourier transform of  $p'$  and  $f'$ , respectively, and  $k^2 = k_x^2 + k_y^2 + k_z^2$  is the spatial wavenumber, squared. The solution of (4.8) can be obtained using the

corresponding Green's function,

$$G(t, t') = \frac{1}{c_o k} \sin c_o k(t - t'). \quad (4.9)$$

Then,

$$\begin{aligned} \hat{p}(t) &= \frac{c_o}{k} \int_0^t \hat{f}(t') \sin c_o k(t - t') dt' \\ &= \frac{c_o}{k} \int_0^t \hat{f}(t - \tau) \sin(c_o k \tau) d\tau. \end{aligned} \quad (4.10)$$

In order to express the effect of  $c_o$ , and consequently  $M_c$ , on the pressure-strain, the spectral density of the pressure-strain,  $\Psi_{ij}(\mathbf{k})$ , is introduced. The term  $\Psi_{ij}(\mathbf{k})$  and the two-point pressure-strain correlation,  $\Pi_{ij}(\mathbf{r})$ , constitute a Fourier transform pair as follows:

$$\begin{aligned} \Pi_{ij}(\mathbf{r}) &= \overline{p'(\mathbf{x} + \mathbf{r})(u''_{i,j}(\mathbf{x}) + u''_{j,i}(\mathbf{x}))} \\ &= \int_{-\infty}^{\infty} \Psi_{ij}(\mathbf{k}) e^{i\mathbf{k} \cdot \mathbf{r}} d\mathbf{k}. \end{aligned} \quad (4.11)$$

Note that  $\Pi_{ij}(\mathbf{r} = 0)$  is the pressure-strain correlation in the Reynolds stress transport equations and, from (4.11), is given by

$$\Pi_{ij} = \overline{p'(u''_{i,j} + u''_{j,i})} = \int_{-\infty}^{\infty} \Psi_{ij}(\mathbf{k}) d\mathbf{k}. \quad (4.12)$$

The pressure-strain spectral density,  $\Psi_{ij}(\mathbf{k})$ , can be related to the Fourier transforms of the pressure fluctuations and the velocity fluctuations by

$$\Psi_{ij}(\mathbf{k}) = \frac{(2\pi)^3}{2V} (\hat{p}(\hat{u}_{i,j}^* + \hat{u}_{j,i}^*) + \hat{p}^*(\hat{u}_{i,j} + \hat{u}_{j,i})), \quad (4.13)$$

where  $V$  is the volume of the turbulent region being considered. Substituting (4.10) for  $\hat{p}(t)$  into (4.13) gives

$$\Psi_{ij}(\mathbf{k}) = \frac{c_o(2\pi)^3}{2Vk} \int_0^t (\hat{f}(t - \tau)(\hat{u}_{i,j}^* + \hat{u}_{j,i}^*) + \hat{f}^*(t - \tau)(\hat{u}_{i,j} + \hat{u}_{j,i})) \sin(c_o k \tau) d\tau. \quad (4.14)$$

For statistically stationary turbulence ( $t \rightarrow \infty$ ), the term between large parentheses can be defined as a function,  $\hat{F}_{ij}(\tau, \mathbf{k})$ , and in the asymptotic limit,  $t \rightarrow \infty$ , we have

$$\Psi_{ij}(\mathbf{k}) = \frac{c_o(2\pi)^3}{2Vk} \int_0^{\infty} \hat{F}_{ij}(\tau, \mathbf{k}) \sin(c_o k \tau) d\tau. \quad (4.15)$$

In order to obtain an estimate for the effect of compressibility on the pressure-strain, we account for the temporal decorrelation typical of turbulence by

$$\hat{F}_{ij}(\tau, \mathbf{k}) = \hat{F}_{ij}(\mathbf{k}) e^{-\tau/\tau_I}, \quad (4.16)$$

where  $\tau_I$  is a characteristic decorrelation time. It follows that

$$\Psi_{ij}(\mathbf{k}) = \frac{c_o(2\pi)^3 \hat{F}_{ij}(\mathbf{k})}{2Vk} \int_0^{\infty} e^{-\tau/\tau_I} \sin(c_o k \tau) d\tau = \frac{(2\pi)^3 \hat{F}_{ij}(\mathbf{k})}{2Vk^2} \frac{1}{1 + 1/(c_o k \tau_I)^2}. \quad (4.17)$$

The first term in (4.8) drops out in the incompressible limit,  $c_o \rightarrow \infty$ , giving  $\hat{p} = \hat{f}/k^2$ .

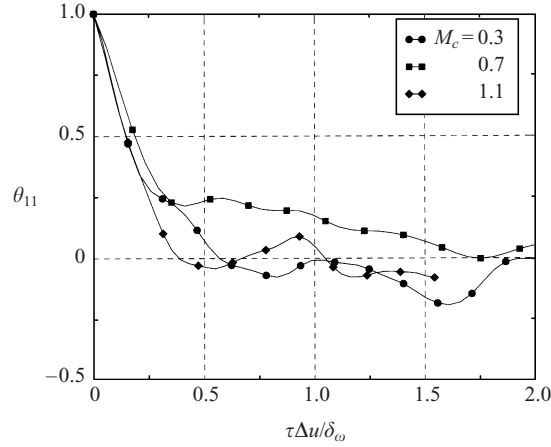


FIGURE 12. Two-time correlation,  $\theta_{11}(0, \tau)$ , at the centreplane as a function of Mach number.

Therefore, it is possible to express the incompressible form of the spectral pressure–strain density as

$$\Psi_{ij}^I(\mathbf{k}) = \frac{(2\pi)^3 \hat{F}_{ij}(\mathbf{k})}{2Vk^2} \quad (4.18)$$

so that (4.17) becomes

$$\Psi_{ij}(\mathbf{k}) = \frac{\Psi_{ij}^I(\mathbf{k})}{1 + 1/(c_o k \tau_I)^2}. \quad (4.19)$$

In the incompressible limit,  $c_o \rightarrow \infty$ , (4.19) predicts that  $\Psi_{ij}(\mathbf{k}) \rightarrow \Psi_{ij}^I(\mathbf{k})$ , as expected. For finite speed of sound,  $\Psi_{ij}(\mathbf{k})$  always decreases with respect to  $\Psi_{ij}^I(\mathbf{k})$ . Integrating over all wavenumber vectors,  $\mathbf{k}$ , the following expression for the pressure–strain is obtained:

$$\frac{\Pi_{ij}}{\Pi_{ij}^I} = 1 - \frac{1}{\Pi_{ij}^I} \int_{-\infty}^{\infty} \frac{\Psi_{ij}^I(\mathbf{k})}{1 + (c_o \tau_I k)^2} d\mathbf{k}. \quad (4.20)$$

Thus, (4.20) is the major result of this analysis, namely, all components of the pressure–strain tensor show *monotone decrease* with increasing speed of sound in compressible shear flow. The assumptions of the analysis are: first, the turbulence field at the centreplane is quasi-homogeneous and, second, the two-time correlation of  $f'$  and  $s'_{ij}$  exhibits decorrelation which, of course, is a typical feature of turbulent flow. The specific form of the pressure–strain decrease with increasing  $M_c$  that is given by (4.20) follows from our choice of the simple model,  $e^{-\tau/\tau_I}$ , to represent temporal decorrelation. The consequence of other possible choices for the temporal decorrelation function is explored in Appendix B. Figure 12 shows representative plots of the two-time correlation  $\theta_{11}(0, \tau)$ , where

$$\theta_{ij}(\mathbf{r}, \tau) = \overline{f'(\mathbf{x} + \mathbf{r}, t - \tau)(u'_{i,j} + u'_{j,i})(\mathbf{x}, t)}. \quad (4.21)$$

Notice that  $\theta_{ij}(\mathbf{r}, \tau)$ , as defined above, and  $\hat{F}_{ij}(\mathbf{k}, \tau)$  constitute a Fourier transform pair in the same way as  $\Pi_{ij}(\mathbf{r})$  and  $\Psi_{ij}(\mathbf{k})$ . It is clear that DNS supports our assumption of temporal decorrelation. Figure 11 shows DNS results regarding the integrated pressure–strain, normalized with the corresponding incompressible value, as a function of  $M_c$ . The  $\bar{\Pi}_{33}$  component shows the same behaviour since the pressure–dilatation is much smaller in these simulations, requiring as a first approximation that

$\bar{\Pi}_{11} + \bar{\Pi}_{22} + \bar{\Pi}_{33} \simeq 0$ . As can be seen, all three components,  $\bar{\Pi}_{11}$ ,  $\bar{\Pi}_{22}$  and  $\bar{\Pi}_{12}$ , decrease as a function of  $M_c$  as shown by the preceding analysis. Further insight can be obtained by studying asymptotic limits of (4.20) for both low and high sound speeds, respectively. First, consider flow speeds low with respect to that of sound, that is  $(c_o \tau_l k)^2 \gg 1$ , giving

$$\frac{\Pi_{ij}}{\Pi_{ij}^I} = 1 - \frac{1}{(c_o \tau_l)^2} \frac{\int_{-\infty}^{\infty} \Psi_{ij}^I(\mathbf{k})/k^2 d\mathbf{k}}{\int_{-\infty}^{\infty} \Psi_{ij}^I(\mathbf{k}) d\mathbf{k}}. \quad (4.22)$$

Here, the ratio of the two integrals has dimensions of length squared and, to a first approximation, can be taken to be  $l^2$  where  $l$  is a single characteristic length scale assumed to be associated with all components of the two-point, pressure–strain correlation tensor. Thus,

$$\frac{\Pi_{ij}}{\Pi_{ij}^I} = 1 - \frac{l^2}{(c_o \tau_l)^2}. \quad (4.23)$$

There are two important inverse time scales of the flow:  $S = |\partial \bar{u}_1 / \partial x_2|$  imposed by the mean flow and  $l/u$  associated with the velocity fluctuation. The model for  $\tau_l$ ,

$$\frac{1}{\tau_l^2} = \alpha_1^2 S^2 + \alpha_2^2 u^2 / l^2 + \alpha_3 S u / l, \quad (4.24)$$

is the simplest model for the time scale that satisfies the following constraints. First, in the absence of mean shear,  $\tau_l$  is proportional to the turbulence time scale,  $l/u$ . Second, in the case of very large mean shear,  $\tau_l$  approaches the distortion time scale,  $1/S$ . Third, in the case of flow with a given shear, the time scale can increase (decrease) with increasing turbulence fluctuations corresponding to negative (positive)  $\alpha_3$ . Note that although  $\alpha_3$  can be negative, it is constrained so that the overall sum on the right-hand side of (4.24) is positive.

After substituting (4.24) into (4.23), the pressure–strain term in the low-Mach-number limit becomes

$$\frac{\Pi_{ij}}{\Pi_{ij}^I} = 1 - (\beta_1^2 M_g^2 + \beta_2^2 M_t^2 + \beta_3 M_g M_t), \quad (4.25)$$

where  $M_g = Sl/c_o$  is the gradient Mach number and  $M_t = u/c_o$  is the turbulent Mach number. Note that the term in brackets on the right-hand side must be positive since it is a model for the positive quantity,  $l^2/(c_o^2 \tau_l^2)$ . In the case of uniformly sheared flow, the gradient Mach number was used by Sarkar (1995) as the primary determinant of reduced turbulent production and thereby reduced turbulent kinetic energy. The present analysis shows that the pressure–strain correlation must depend on  $M_g$ . The specific functional form, (4.25), is a consequence of the simplest possible model, (4.24), for the characteristic decorrelation time.

The implications of (4.23) are even simpler for the mixing layer in self-similar conditions when, by definition,  $l/(\tau_l \Delta U)$  is constant at the centreline. The constant could depend on the Mach number; however, for small values of Mach number, we assume that  $l/(\tau_l \Delta U)$  is independent of Mach number leading to the following expression:

$$\frac{\Pi_{ij}}{\Pi_{ij}^I} = 1 - K_0 M_c^2 \quad (4.26)$$

that describes the leading-order influence of compressibility at low Mach number.

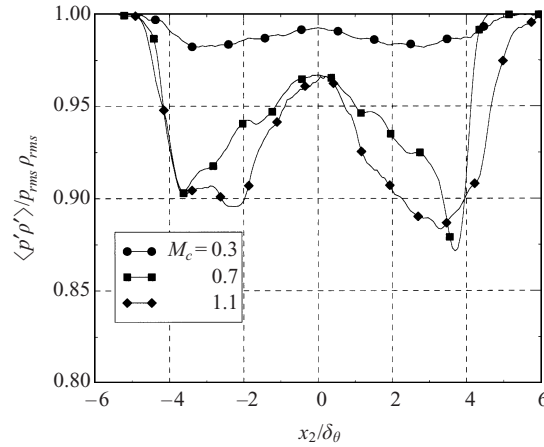


FIGURE 13. Correlation between pressure fluctuations and density fluctuations at different convective Mach numbers as a function of  $x_2/\delta_\theta$ .

A similar analysis can be carried out to obtain the other limit where flow speeds large with respect to that of sound are considered, that is  $(c_o \tau_I k)^2 \ll 1$ . The asymptotic solution is

$$\frac{\Pi_{ij}}{\Pi_{ij}^I} = \frac{1}{K_\infty M_c^2}, \quad (4.27)$$

where the constants  $K_0$  and  $K_\infty$  must be calculated from data.

The wave equation, (4.7), for the pressure is a useful approximation for analysis of cases with moderate Mach number and is consistent with the energy equation, (2.3), if the heat conduction and viscous dissipation terms are assumed negligible and the isentropic relation is assumed. A consequence of the isentropic relationship used to derive the wave equation is that the cross-correlation coefficient between density and pressure is unity. Figure 13 shows the pressure–density fluctuation correlation across the shear layer as a function of  $M_c$ . It can be observed that pressure and density fluctuations are well correlated up to the largest convective Mach number investigated in this study. The agreement is best for the low convective Mach number case and in general at the centre of the shear layer. The largest departure from unity at the centre of the shear layer is approximately 3%. Thus, the assumption of linear dependence of pressure fluctuations on density fluctuations is well supported for the range of  $M_c$  studied here.

At high Mach numbers,  $M_c \gg 1$ , the general thermodynamic relation must be used,

$$\frac{Dp}{Dt} = \left( \frac{dp}{d\rho} \right)_s \frac{D\rho}{Dt} + \left( \frac{dp}{ds} \right)_\rho \frac{Ds}{Dt}, \quad (4.28)$$

where the first term on the right-hand side is the ‘acoustic’ contribution and the second term is the ‘entropy’ contribution. Indeed, by taking the time derivative of (4.28) and using the divergence of the momentum equation, a modified wave equation for the pressure fluctuation results which involves entropy fluctuations and is valid for all Mach numbers. For our purpose, it is enough to estimate the contribution of the ‘entropy’ mode when it dominates the ‘acoustic’ mode. This can be done by considering the limit  $M_c \gg 1$ , when the second term on the right-hand side of (4.28)

dominates and, consequently, (2.3) for the pressure becomes

$$\frac{\partial p}{\partial t} + u_k \frac{\partial p}{\partial x_k} = \gamma \frac{\partial}{\partial x_k} \left( \frac{1}{RePr} \frac{\partial}{\partial x_k} \left( \frac{p}{\rho} \right) \right) + (\gamma - 1)\phi. \quad (4.29)$$

Thus, fluctuations in the pressure field are related to those in the dissipation rate,  $\phi = \tau_{ij}u_{i,j}$ , and when  $M_c \gg 1$  the pressure and pressure–strain terms do not vanish, which is a physically consistent result.

An order of magnitude analysis of (4.29) in the shear layer (characteristic velocity,  $\Delta u$ , and characteristic length,  $\delta_\theta$ ) gives

$$p' \frac{\Delta u}{\delta_\theta} = O(\rho_o \epsilon) = \alpha_1 \rho_o \frac{\Delta u^3}{\delta_\theta}, \quad (4.30)$$

which suggests that the pressure fluctuations can be estimated by

$$p' = \alpha_1 \rho_o \Delta u^2 \quad (4.31)$$

and the asymptotic value of the pressure–strain,  $\Pi_{ij}^\infty$ , by

$$\Pi_{ij}^\infty = \alpha_2 \rho_o \frac{\Delta u^3}{\delta_\theta}. \quad (4.32)$$

Finally, the pressure–strain normalized by its incompressible value approaches a constant when  $M_c \gg 1$ , that is,

$$\frac{\Pi_{ij}^\infty}{\Pi_{ij}^I} = \alpha_3, \quad (4.33)$$

where  $\alpha_3$  is a constant.

It is remarkable that the main effect of compressibility on the pressure–strain correlation in shear flows can be obtained without knowledge of the exact shape of  $\Psi_{ij}^I$  (which is quite complicated). This result is applicable to  $\Pi_{11}$  and not to  $\epsilon_{11}$ , the other term that contributes to (4.5) for the growth rate. DNS results have shown that  $\epsilon_{11}$  does not change strongly with  $M_c$ . Since  $\Pi_{ij}$  progressively decreases with  $M_c$ , approaching a constant value for sufficiently large  $M_c$ , the term  $\epsilon_{11} - \Pi_{11}^\infty$  dominates in (4.5) resulting in an asymptotic, non-zero growth rate for  $M_c \gg 1$ .

So far, qualitative insights into the effect of  $M_c$  on the pressure–strain term have been obtained using analysis. Now we turn to modelling the pressure–strain so as to quantitatively capture the experimentally observed influence of  $M_c$  on the growth rate. The following pressure–strain model has the asymptotic behaviour of (4.26)–(4.27) that has been derived by analysis of the wave equation, and follows (4.33) at large  $M_c$  when entropy fluctuations dominate:

$$\frac{\Pi_{ij}}{\Pi_{ij}^I} = (1 - c) \frac{1 + aM_c^2 \exp(-(2M_c - 1/2)^2)}{1 + bM_c^2} + c. \quad (4.34)$$

Since the experimental data report the normalized growth rate, the pressure–strain correlation needs to be inferred by using (4.5). The data from the ‘Langley Experimental Curve’ are used to fit (4.34) together with a constant value for  $Q(z) = 1.1$  and  $\bar{\epsilon}_{11}/(\bar{\epsilon}_{11}^I - \bar{\Pi}_{11}^I) = 0.25$ . The parameters of the model are  $a = 4.0$ ,  $b = 4.1$  and  $c = 0.091$ . As can be seen, this expression has the correct behaviour at low and high Mach numbers. From (4.34), the constants appearing in (4.26)–(4.27) are calculated to be  $K_0 = 0.89$  and  $K_\infty = 4.5$ . Figure 14 shows that (4.34) is a good fit to the ‘experimental’ pressure–strain ratio.

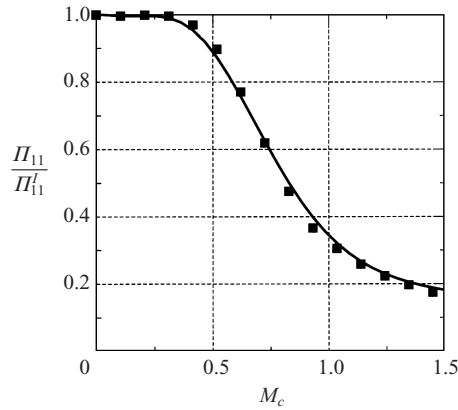


FIGURE 14. Pressure–strain ratio. Symbols: data deduced from the ‘Langley Experimental Curve’ and line: equation (4.34).

## 5. Anisotropy of the Reynolds stress

The Reynolds stress anisotropy defined by

$$b_{ij} = \frac{R_{ij} - \frac{2}{3}K\delta_{ij}}{2K} \quad (5.1)$$

is an important characteristic of the velocity fluctuations that is used in advanced modelling of turbulent flows. As discussed in the introduction, some studies observe only small changes in the diagonal components of  $b_{ij}$  while other studies find increased magnitude of  $b_{11}$ ,  $b_{22}$ , and  $b_{33}$  because  $R_{22}$  and  $R_{33}$  decrease more than  $R_{11}$  as a function of  $M_c$ . Similarly, there is disagreement with respect to the effect of compressibility on  $b_{12}$ .

Figures 15(a), 15(b) and 15(c) show the temporal evolution of the anisotropy tensor, obtained by integrating  $R_{ij}$  and  $K$  along the shear layer and then using (5.1), for different  $M_c$ . Two important conclusions are drawn from these figures. First, during its initial evolution, the anisotropy tensor is strongly affected by  $M_c$ , whereby larger magnitudes of the diagonal components of  $b_{ij}$  are measured for increasing  $M_c$ . Table 4 illustrates this trend using the peak anisotropies during the early-time transient. Second, after sufficiently long time, the anisotropy tensor approaches asymptotic values that are weakly dependent on  $M_c$ . Table 4 also shows values from the self-similar region, where a weak increase of the normal stress anisotropies with  $M_c$  is observed while the off-diagonal component  $b_{12}$  remains constant. The peak values of turbulence intensities and shear stress at the centre of the shear layer can also be considered and are preferable in comparing with experimental data. Table 5, which shows the normalized turbulence intensities, compares cases A3, A7 and A11 with experimental studies by Bell & Mehta (1990), Samimy & Elliot (1990) and Chambres *et al.* (1998). The ratios  $\sqrt{R_{22}/R_{11}}$  and  $\sqrt{R_{12}/R_{11}}$  are measures of anisotropy, and as can be seen they do not change considerably between cases. The conclusion from these experiments and DNS is that the effect of compressibility on  $b_{ij}$  is weak.

Previous DNS studies by Vreman *et al.* (1996) and Freund *et al.* (2000) observed increased values of normal stress anisotropy with  $M_c$ . The  $M_c = 1.2$  case of Vreman *et al.* (1996) was conducted up to  $\tau \simeq 1000$  but started with a single pair of oblique modes while that of Freund *et al.* (2000) used broadband initial fluctuations but followed the evolution only up to  $\tau \simeq 350$ . It is possible that the turbulence was not

---

$M_c$	Peak			Long-time		
	$b_{11}$	$b_{22}$	$b_{12}$	$b_{11}$	$b_{22}$	$b_{12}$
0.3	0.26	-0.16	0.19	0.14	-0.06	0.18
0.7	0.29	-0.19	0.19	0.15	-0.10	0.15
1.1	0.36	-0.22	0.18	0.14	-0.10	0.16

---

TABLE 4. Reynolds stress anisotropy: peak values during its early-time evolution and long-time values.

---

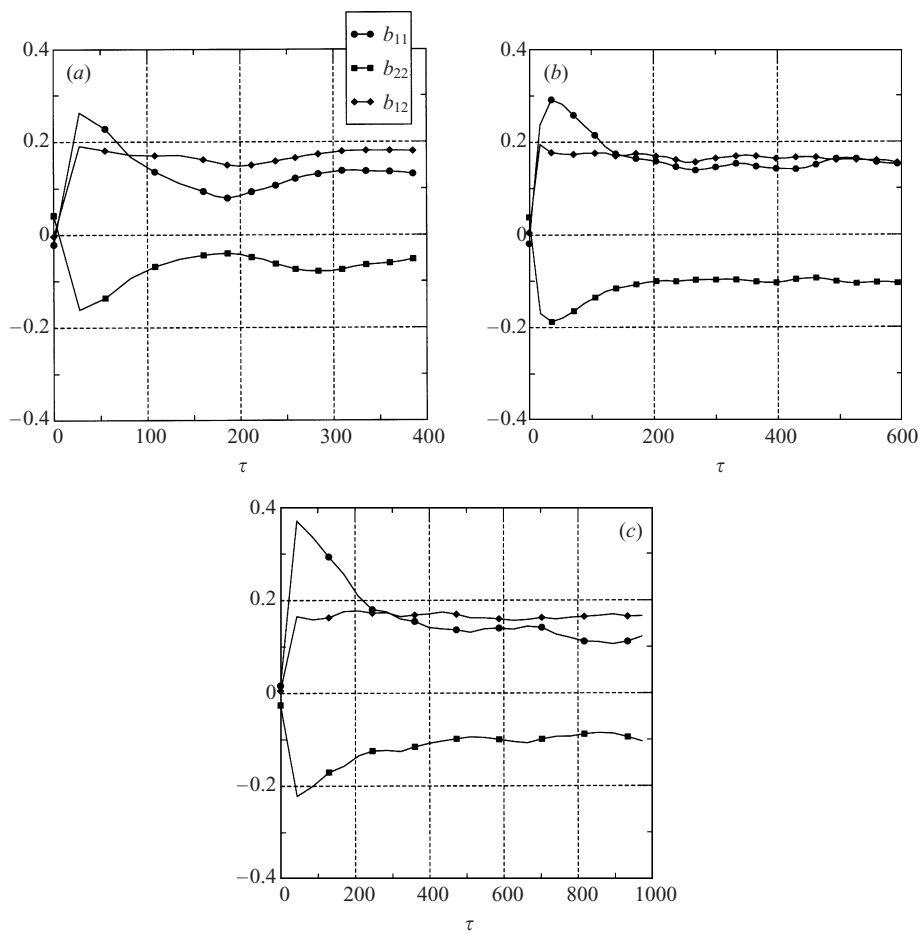


FIGURE 15. Anisotropy tensor evolution for (a)  $M_c = 0.3$ , (b)  $M_c = 0.7$  and (c)  $M_c = 1.1$ .

in a fully developed, self-similar state in these studies and the finding of increased normal stress anisotropy with  $M_c$  in these studies is analogous to the increased levels seen at early time in our DNS. We also note that transitional shear flows or developing shear flows ( $P/\epsilon$  larger than equilibrium values) can be expected to have values of  $R_{11}$ , relative to  $R_{22}$  and  $R_{33}$ , which are higher than in equilibrium shear flow with self-similar turbulence statistics due to a higher relative importance of linear effects.

	$M_c$	$\sqrt{R_{11}}/\Delta u$	$\sqrt{R_{22}}/\Delta u$	$\sqrt{R_{12}}/\Delta u$	$\sqrt{R_{22}/R_{11}}$	$\sqrt{R_{12}/R_{11}}$
Bell & Mehta (1990)	0.0	0.18	0.14	0.10	0.777	0.555
Present DNS	0.3	0.17	0.134	0.103	0.788	0.606
Samimy & Elliot (1990)	0.64	0.15	0.10	0.088	0.666	0.586
Present DNS	0.7	0.153	0.103	0.087	0.673	0.568
Chambres <i>et al.</i> (1998)	1.0	0.14	0.085	0.083	0.607	0.592
Present DNS	1.1	0.141	0.095	0.083	0.674	0.588

TABLE 5. Comparison of peak turbulent intensities in experiments and DNS.

## 6. Density effect on the growth rate

The aim of series B is the study of the effect of density ratio on the growth rate. In this series, two parameters have been kept constant, the convective Mach number,  $M_c$ , and the average density,  $\rho_o = (\rho_1 + \rho_2)/2$ . Results corresponding to  $s = \rho_2/\rho_1 = 2, 4$  and  $8$  are shown. Note that  $s > 1$  implies that the upper stream has the lower density. It can be shown that the average equations and boundary conditions are invariant under the change  $x_2 \rightarrow -x_2$ ,  $u_1 \rightarrow -u_1$  and  $u_2 \rightarrow -u_2$  from where the invariance of the results to the change  $s \rightarrow 1/s$  is immediately clear. The influence of the density ratio on temporal growth rates of the vorticity thickness, related to the mean streamwise velocity profile, as well as the momentum thickness, related to the profiles of turbulent Reynolds stress  $R_{12}$  and the mean density  $\bar{\rho}$ , is investigated.

From similarity arguments, Brown (1974) derived an expression for the vorticity thickness growth rate dependence on the velocity and density ratios. The growth rate in a frame moving with the convection velocity,  $U_c$ , is defined by

$$\frac{1}{\Delta u} \frac{d\delta_\omega}{dt} = \dot{\delta}_\omega = \frac{C_\delta}{2}. \quad (6.1)$$

Brown (1974) states that, although  $C_\delta$  can be assumed independent of  $s$ , based on limited data available for low-speed flow, the convection velocity,  $U_c$ , shifts to the velocity of the high-density stream. Therefore, the spatial growth rate is modified by unequal free-stream densities, although the temporal growth rate,  $C_\delta$ , is not. Brown (1974) found that the expression

$$\frac{d\delta_\omega}{dx} = C_\delta \frac{(1-r)(1+s^{1/2})}{2(1+rs^{1/2})} \quad (6.2)$$

matched experimental data with  $r = u_2/u_1$  the velocity ratio,  $s = \rho_2/\rho_1$  the density ratio, and subscript 1 denoting the high-speed stream. Equation (6.2) was further improved by Dimotakis (1984) by accounting for the feature of asymmetric entrainment associated with a spatially developing shear layer that cannot be captured by the temporal model. Since the current DNS corresponds to a temporally evolving flow in a reference frame mandated to move with the mean velocity  $(U_1 + U_2)/2$ , conclusions can be drawn with respect to the effect of  $s$  on solely  $C_\delta$  and not  $U_c$ . Table 6 gives the values of  $C_\delta$  for various density ratios and  $M_c = 0.7$ . A decrease of  $C_\delta$  with increasing  $s$  is observed.

The penultimate column of table 6 shows the momentum thickness growth rate normalized by its constant-density value. A large decrease of  $\dot{\delta}_\theta$  with increasing  $M_c$  is seen. The dependence of momentum thickness growth rate on  $s$  is much stronger than that of vorticity thickness growth rate.

To calculate the effect of the density ratio on the momentum thickness growth rate,

$s$	$C_\delta$	$a(s)$	$\dot{\delta}_\theta/\dot{\delta}_{\theta,1}$	$1 - \lambda(s)a(s)$
1	0.117	0.00	1.00	1.00
2	0.084	0.52	0.67	0.82
4	0.093	0.70	0.57	0.58
8	0.071	0.88	0.37	0.32

TABLE 6. Dependence on  $s$  of  $C_\delta$ ,  $a(s)$  and growth rate ratio for  $M_c = 0.7$ .

the definition of  $\dot{\delta}_\theta$  is studied, where (3.10) is now written in terms of  $\tilde{u}_1$ ,

$$\dot{\delta}_\theta = -\frac{2}{\rho_o \Delta u^3} \int_{\Delta u/2}^{-\Delta u/2} \bar{\rho} R_{12} d\tilde{u}_1. \quad (6.3)$$

The mean density as well as the Reynolds stress can be expressed in terms of the mean streamwise velocity. This transformation is very convenient since the shear layer centre, defined in the customary form by the dividing streamline position, is recovered directly at the point  $\tilde{u}_1 = 0$ . The self-similar coordinate of the shear layer centre can equivalently be obtained by setting the right-hand side of (3.19) to zero. Denoting the centre of the shear layer by  $\eta_c$ , the condition to be satisfied by  $\hat{u}_2$  is

$$\hat{u}_2(\eta_c) - \eta_c = 0. \quad (6.4)$$

Equation (6.4) implies that the dividing centreline is not at necessarily  $\eta = 0$ . To obtain the direction of the shift, (3.16) is integrated from  $-\infty$  to  $\eta_c$ , imposing  $\hat{u}_2(-\infty) = 0$ ,

$$\eta_c = \frac{1}{\hat{\rho}(\eta_c)} \int_{-\infty}^{\eta_c} \eta \frac{d\hat{\rho}}{d\eta} d\eta. \quad (6.5)$$

It can be seen that since  $s > 1$  for the cases discussed here,  $d\hat{\rho}/d\eta < 0$  for all  $\eta$ , implying that  $\eta_c$  must be positive. This simple argument explains why the shear layer shifts in one direction, and also explains that the shift is a result of the variable density. Figure 16 shows the mean density and velocity profiles for  $s = 2, 4$  and  $8$ . The shear layer centre, ( $\hat{u}_1 = 0$ ), shifts upward to positive  $\eta$ . When the density ratio is changed from  $s$  to  $1/s$ , the shear layer centre shifts downward by an equal amount to negative  $\eta$  according to (6.5). In summary, the shear layer centre shifts to the lower density side.

In order to quantify the density effect on the momentum thickness growth rate, the functional form  $\bar{\rho}(\tilde{u}_1)$  is now obtained. At  $t = 0$ , the density and velocity profiles have the same hyperbolic tangent variation between their free-stream values. Therefore, at  $t = 0$ ,

$$\bar{\rho} = \rho_o(1 + 2\lambda\hat{u}_1), \quad (6.6)$$

where  $\hat{u}_1 = \tilde{u}_1/\Delta u$  and  $\lambda(s)$  is defined by (2.11). It can be verified that  $\lambda$  is such that  $\bar{\rho} = \rho_1$  at  $\tilde{u}_1 = -\Delta u/2$  and  $\bar{\rho} = \rho_2$  at  $\tilde{u}_1 = \Delta u/2$ . At later time, the dividing centreline,  $\hat{u}_1 = 0$ , shifts with respect to the position of average density  $\rho_o = (\rho_1 + \rho_2)/2$  and this shift depends on the value of  $s$ . Therefore, (6.6) is modified as follows:

$$\bar{\rho} = \rho_o[1 + \lambda(2\hat{u}_1 - a(s)f(\hat{u}_1))]. \quad (6.7)$$

The specified density at the free streams require that  $f(-1/2) = f(1/2) = 0$ . Furthermore,  $f(\hat{u}_1)$  is defined as a positive quantity with a maximum value of 1. The unknown function  $a(s)$  accounts for the magnitude of the shift between the velocity

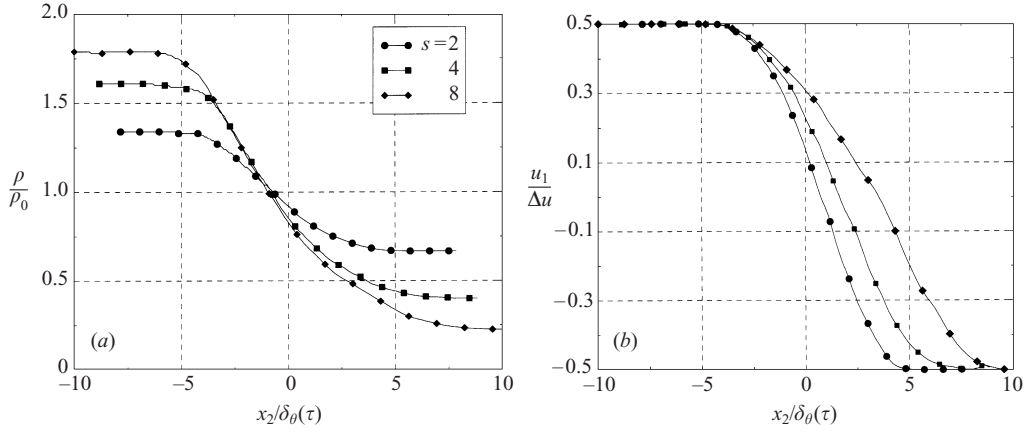


FIGURE 16. (a) Mean density and (b) streamwise velocity profiles.

and density profiles, and is calculated from the DNS database, giving a quantity of order one. Note that the preceding analysis and DNS observations show that the dividing streamline moves to the low-density side, that is,  $\bar{\rho}(s, \hat{u}_1 = 0) < \rho_0$ , which implies that

$$\lambda(s)a(s) > 0 \quad (6.8)$$

for all values of density ratio,  $s \neq 1$ . Due to the symmetry of the equations mentioned at the beginning of the section,  $\lambda(s)a(s) = \lambda(1/s)a(1/s)$ , giving  $a(s) = -a(1/s)$ . The calculation of  $a(s)$  is done simply by using (6.7), where

$$a(s) = 2\hat{u}_{1,max} - \frac{\hat{\rho}(\hat{u}_{1,max}) - 1}{\lambda}. \quad (6.9)$$

Here,  $\hat{u}_{1,max}$  is the value at which  $f(\hat{u}_1)$  is maximized, i.e.  $f'(\hat{u}_{1,max}) = 0$  or, equivalently, using (6.7),

$$\frac{d\hat{\rho}}{d\hat{u}_1}(\hat{u}_{1,max}) = 2\lambda. \quad (6.10)$$

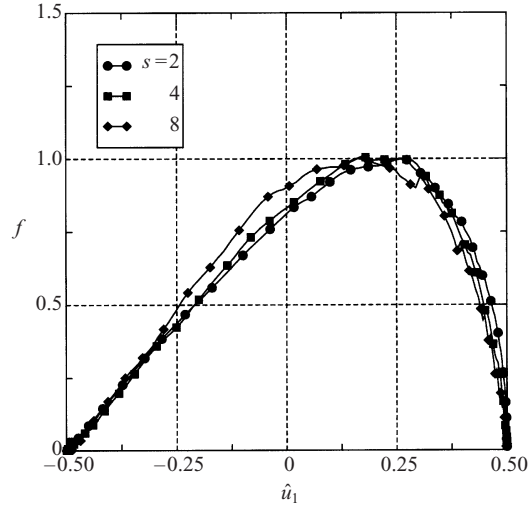
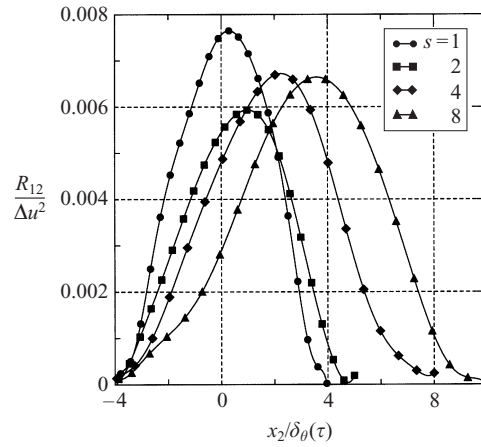
Figure 17 shows the function  $f(\hat{u}_1)$ , obtained by calculating  $a(s)$  from the DNS database and table 6 shows the measured values of  $a(s)$ .

The functional dependence of  $R_{12}$  on the velocity profile is now obtained. Figure 18 shows self-similar profiles of  $R_{12}$  at different values of  $s$  for constant convective Mach number. As can be seen, there is little change in the peak magnitude of the Reynolds stress but there is a shift to the low-density side, associated with the shift of the dividing streamline. This suggests the following functional form for  $R_{12}$ :

$$R_{12} = \Delta u^2 \dot{\delta}_{\theta,1} g(\hat{u}_1), \quad (6.11)$$

where  $\dot{\delta}_{\theta,1}$  is the momentum thickness growth rate corresponding to the same Mach number and density ratio,  $s = 1$ . The function  $g(\hat{u}_1)$  is shown in figure 19 for cases B2, B4 and B8. Finally (6.3) can be written in terms of the new functions, giving

$$\frac{\dot{\delta}_\theta}{\dot{\delta}_{\theta,1}} = 2 \int_{-1/2}^{1/2} [1 + \lambda(s)(2\hat{u}_1 - a(s)f(\hat{u}_1))] g(\hat{u}_1) d\hat{u}_1. \quad (6.12)$$

FIGURE 17. Density function  $f(\hat{u}_1)$ .FIGURE 18. Reynolds stress  $R_{12}$  at  $M_c = 0.7$  for different density ratios.

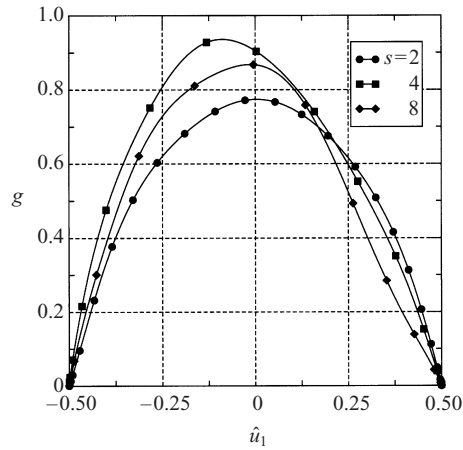
The integral is decomposed into three parts:

$$\frac{\delta_\theta}{\delta_{\theta,1}} = 2 \int_{-1/2}^{1/2} g(\hat{u}_1) d\hat{u}_1 + 4\lambda(s) \int_{-1/2}^{1/2} \hat{u}_1 g(\hat{u}_1) d\hat{u}_1 - 2\lambda(s)a(s) \int_{-1/2}^{1/2} f(\hat{u}_1)g(\hat{u}_1) d\hat{u}_1 \quad (6.13)$$

Since  $\lambda(s = 1) = 0$  and, by definition,  $\delta_\theta(s = 1) = \delta_{\theta,1}$ , the first integral on the right-hand side of (6.13) must be unity. The second integral can be neglected since it is a product of an antisymmetric function by an almost symmetric function and its value is numerically found to be negligible. From our DNS database the error induced by neglecting this second integral is bounded to approximately  $0.08\lambda(s)$  for all cases. Since  $\lambda(s)$  is limited for  $0 < s < \infty$  to

$$0 \leq |\lambda(s)| < 1,$$

the error introduced by neglecting the second integral is approximately 8%. Finally,

FIGURE 19. Reynolds stress function  $g(\hat{u}_1)$ .

the last integral is obtained numerically to be approximately 0.5, resulting in the final expression

$$\frac{\dot{\delta}_\theta}{\dot{\delta}_{\theta,1}} = 1 - \lambda(s)a(s). \quad (6.14)$$

Table 6 shows that (6.14) is a good approximation to the observed effect of density ratio on the momentum thickness growth rate.

The following conclusions can be drawn from (6.14). First, since  $\lambda(s)a(s) > 0$  according to (6.8), the momentum thickness growth rate for the temporally evolving shear layer is always reduced in the case of unequal free-stream densities. In other words, the shift of the dividing streamline to the low-density side is responsible for the decreased growth rate of the momentum thickness. Second, since  $\lambda(s)a(s)$  is invariant under the change  $s \rightarrow 1/s$ , the momentum thickness asymptotic value is unchanged if the densities of the upper and lower streams are interchanged.

## 7. Conclusions

The shear layer between two streams with velocity and density contrasts is studied using DNS. In one series of simulations, the density ratio,  $s = \rho_2/\rho_1$ , is held constant while the convective Mach number,  $M_c$ , is varied between subsonic and supersonic values. In another set of simulations,  $M_c$  is held constant at a high value and  $s$  varied. Large computational domains, large computational grids, and broadband initial conditions ensure that the application of a high-order numerical scheme results in a simulated flow that corresponds to full-blown turbulence. The Reynolds number based on vorticity thickness is as large as 13 600. A detailed validation against experimental data is performed and profiles of turbulence intensities are found to agree well with both low and high Mach number datasets. Furthermore, a more stringent test comparing the turbulent kinetic energy budget in the quasi-incompressible  $M_c = 0.3$  case with another independent DNS study of the incompressible shear layer by Rogers & Moser (1994) is performed and good agreement is again obtained.

The compressibility effect of dramatically reduced turbulence levels and growth rate is a well-known phenomenon and is observed in the current DNS. Reduced turbulence production, rather than increased dilatational terms, appears to be directly responsible

for decreased turbulent kinetic energy as first observed by Sarkar (1995) in uniformly sheared flow. Consistent with the relation between momentum thickness growth rate and integrated production established by Vreman *et al.* (1996) for the mixing layer and their finding using DNS, we also find that the reduced turbulence production is directly linked to the reduced growth rate of the momentum thickness. With increasing  $M_c$ , the normalized pressure fluctuations and pressure–strain term are reduced as first shown by Vreman *et al.* (1996) in the mixing layer, thus decreasing the cross-stream intensity  $v^2$ , thereby the Reynolds shear stress  $\overline{uv}$ , and finally the turbulent production term.

Reduction of normalized pressure fluctuations, concomitant reduction of inter-component energy transfer, and suppression of turbulence levels has been observed in other flows with mean shear, for example uniform shear flow by Sarkar (1996) and the annular mixing layer by Freund *et al.* (2000). In non-sheared flows such as irrotational compression studied by Cambon *et al.* (1993), there is a reduction of pressure fluctuations. However, in contrast to compressible shear flows, the turbulent kinetic energy increases in compressed flows due to an increase in dilatational fluctuations.

An analysis of the wave equation that governs pressure fluctuations in compressible flow is performed in order to explain the behaviour of the pressure–strain term. A monotone decrease of the pressure–strain correlation with increasing compressibility is predicted by the analysis. Furthermore, the asymptotic behaviour at small and large Mach numbers is obtained. The gradient Mach number,  $M_g = Sl/c$ , and the turbulent Mach number,  $M_t = u/c$  appear as the principal determinants of compressibility and, in the case of the self-similar shear layer, both can be related to the convective Mach number  $M_c$ . DNS also shows that the pressure–strain correlation exhibits monotone decrease when  $M_c$  increases. The parameter  $M_g$  was identified by Sarkar (1995) to be useful in discriminating between different flows with the same Mach number, for example between strong compressibility effects when  $\Delta U/c = 1.0$  in the shear layer and their lack in the  $M_c = 1.0$  boundary layer.

Based on our analysis and DNS, the following physical reason for the reduction in the pressure–strain term can be identified. The finite speed of sound in compressible flow causes a time delay,  $l/c$ , in the passage of pressure signals across a characteristic eddy length  $l$  and, thus, causes decorrelation between adjacent points in an ‘eddy’. The ratio of acoustic time delay,  $l/c$ , to a characteristic flow time ( $1/S$  or  $l/\Delta U$ ) increases with Mach number ( $M_g = Sl/c$  or  $M_c = \Delta U/2c$ ) and, as clearly shown by the analysis, the resultant increase in decorrelation inhibits the pressure–strain term. As discussed in the introduction, reduced communication between disturbances in high-speed flows has been advanced as a possible physical reason for the stabilizing effect of compressibility. The analysis of the wave equation performed here may be viewed as a mathematical corroboration of how, with increasing speed of sound, the acoustic time delay is effective in reducing the inter-component energy transfer necessary to maintain turbulence in a shear flow.

When the density ratio is varied in the high-speed regime,  $M_c = 0.7$ , it is found that the momentum thickness growth rate decreases substantially as a function of  $s$ . The change of vorticity thickness growth rate with  $s$  is smaller. With increasing values of  $s$ , the maximum shear stress  $\overline{uv}$  decreases somewhat; however, the main effect of variable density is that the location of peak shear stress shifts to the low-density side causing a substantial reduction in the momentum transport,  $\overline{\rho uv}$ . The shift of the location of maximum shear stress or, equivalently, the dividing streamline is a consequence of mean momentum conservation. An analytical expression relating the shift to the momentum thickness growth rate is also derived.

Case	$M_c$	$s$	$L_x \times L_y \times L_z$	$N_x \times N_y \times N_z$
AS3	0.3	1.0	$172 \times 129 \times 86$	$256 \times 192 \times 128$
AS11	1.1	1.0	$172 \times 129 \times 86$	$256 \times 192 \times 128$
AA3	0.3	1.0	$172 \times 129 \times 86$	$384 \times 288 \times 192$

TABLE 7. Parameters for the validation simulations (symbols are as in table 1.)

The variation of turbulence intensities and shear stress with  $M_c$  is examined. Our finding that, in the self-similar state, all components of the turbulence decrease with Mach number with only a weak effect on the anisotropy is in agreement with the experiments of Samimiy & Elliot (1990) and the more recent data of Chambres *et al.* (1998). It should be noted that some experimental and DNS investigations report a substantially larger reduction in the cross-stream component  $\overline{v^2}$  compared to  $\overline{u^2}$ . We find a similar situation during the early developing stage of the shear layer but not, later in the DNS, when the flow field is close to its final self-similar state.

This work was supported by AFOSR through grant F49620-96-1-0106. Computational time was provided by the CEWES and NAVO Major Shared Resource Centers. The authors wish to thank Dr Scott Stanley and Dr Frank Jacobitz for helpful discussions on the numerical method.

## Appendix A. Validation of the simulations

In order to check the accuracy of the results, two-point correlations, spectra and the turbulent kinetic energy balance were investigated. Several additional simulations were also performed to explicitly investigate the effects of domain size, resolution and filter characteristics. All simulations were performed at the same Reynolds number,  $Re = 800$ . Table 7 shows the grid sizes and computational domain lengths corresponding to the additional simulations.

The additional simulations labelled AS3 and AS11 were performed on a domain of streamwise length half that of cases A3 and A11 presented in the paper. The results show that even with this smaller domain size the results are acceptable. Simulation AA3 was performed to study the effect of finer resolution (50% better resolution in each direction).

### A.1. Domain size effect

The evolution of momentum thickness with time is shown in figure 20 for different cases. As can be seen, there are only minor differences between the results of the smaller domain simulations and the larger domain simulations. Even for the large- $M_c$  case the differences are small. Figure 21(a–e) shows the correlations for simulations A3, AS3, A11, AS11 and A7, respectively. In order to eliminate contamination of the results by finite domain size, the correlation should be small for large  $r/\delta_\theta$ . It can be verified that this condition is met for all cases and especially for A3 and A11 which have twice the streamwise domain length relative to the other cases.

We conclude from these results that simulation A7 that was performed in a smaller domain than A3 and A11 is of acceptable quality since little effect on growth evolution is observed between simulations with smaller and larger streamwise domain sizes even though the two-point correlations do not exhibit complete decay to zero decorrelation within the computational domain.

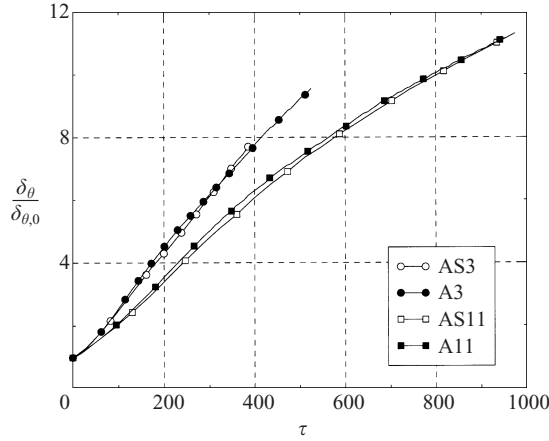


FIGURE 20. Momentum thickness evolution with time for different simulations. Cases AS3 and AS11 have half the streamwise domain length with respect to cases A3 and A11.

### A.2. Resolution

Comparison of the results of Rogers & Moser (1994) and ours in figure 6 is very good for the turbulent production and dissipation terms. Only some differences are observed, away from the centre of the shear layer, for the transport term. Figure 22 shows all the terms in the turbulent kinetic energy budget for simulation A3. The normalized budget of turbulent kinetic energy can be written as

$$\hat{P} - \hat{\epsilon} - \frac{1}{\hat{\rho}} \frac{d\hat{T}_2}{d\eta} - (\hat{u}_2 - \eta) \hat{\delta}_\theta \frac{d\hat{K}}{d\eta} = e \rightarrow 0, \quad (\text{A } 1)$$

where  $K = \Delta u^2 \hat{K}$ . All the terms are shown including the remainder,  $e$ , in (A 1). In general the physical origin of a non-zero  $e$  can be related to a lack of resolution, a lack of measurement points to obtain converged statistics, and deviations from a perfectly self-similar state. It is clear from figure 22 that the remainder,  $e$  is small. Figure 25(b) shows that the dissipation spectrum is well-captured by the grid resolution.

From the above results, it could be concluded that resolution is acceptable. Nevertheless, simulation AA3 was performed with a grid that is 1.5 times finer in each direction to directly ascertain the effect of increased grid resolution. The turbulent field was initialized from the flow field of simulation AS3 at a non-dimensional time of 250, roughly 65% of the total time of simulation AS3, and allowed to evolve from that point up to approximately the same final time. Figure 23 shows the evolution of turbulent kinetic energy with time at the centreplane for simulations AS3 and AA3. As can be seen, the agreement is very good, supporting the fact that the resolution is appropriate.

### A.3. Numerical filter

In order to improve stability of the numerical algorithm for large times the flow variables are filtered using a compact filter. The filtering is performed every  $n$  time steps. The filter parameters are chosen to alter only the high wavenumber part of the spectrum as discussed by Lele (1992). In the present study a fourth-order compact filter is used (C.2.4 of Lele 1992) with coefficient  $\alpha = 0.49$ . The numerical filter step,  $n$ , is such that the dissipation introduced by the filter is minimal. In order to give a quantitative measurement of the filter effect on the flow field, we propose

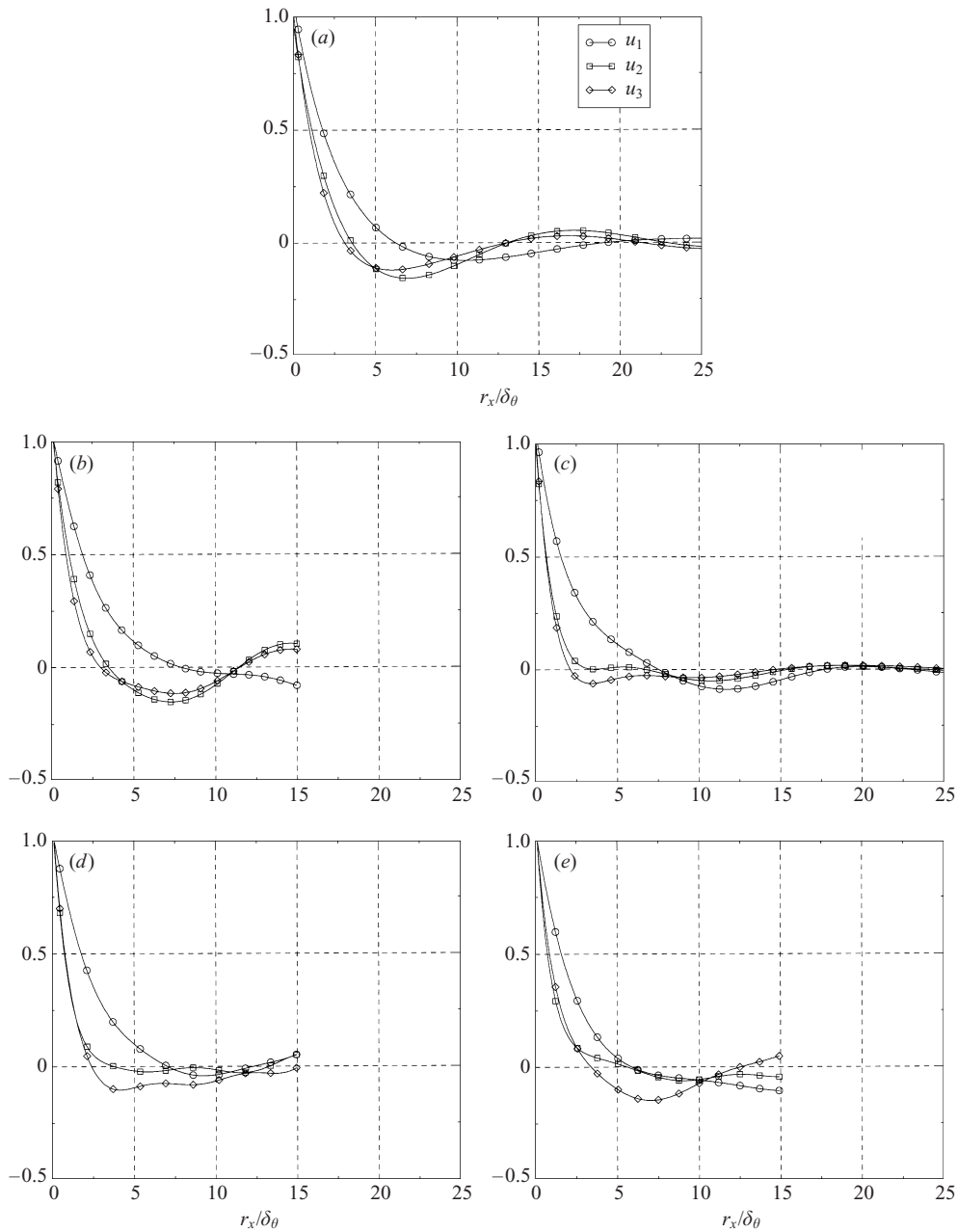


FIGURE 21. Correlations at (a)  $M_c = 0.3$  for simulation A3, normalized time,  $\tau = 500$ ; (b)  $M_c = 0.3$  for AS3,  $\tau = 390$ ; (c)  $M_c = 1.1$  for A11,  $\tau = 850$ ; (d)  $M_c = 1.1$  for AS11,  $\tau = 810$ ; (e)  $M_c = 0.7$  for A7,  $\tau = 550$ .

the following analogy: the use of the filter can be considered to be equivalent to additional numerical dissipation. The difference between the turbulent kinetic energy,  $k$ , before filtering and after filtering,  $k^*$ , at the instant the filter is applied, represents the dissipation due to the filter. The energy removed by filtering is  $k - k^*$ , while the energy removed by viscous dissipation is approximately  $n\Delta t\epsilon$ , where  $n\Delta t$  is the time

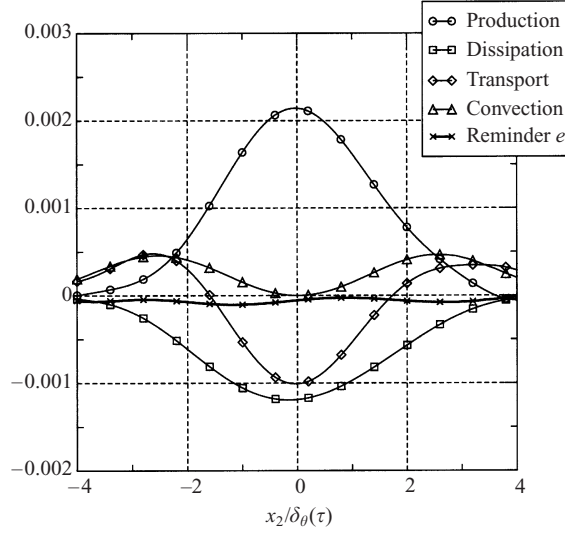


FIGURE 22. Turbulent kinetic energy budget for simulation A3 ( $M_c = 0.3$ ). Production,  $\hat{P}$ , transport,  $(1/\hat{\rho}) d\hat{T}_2/d\eta$ , dissipation,  $\hat{\epsilon}$ , convection,  $(\hat{u}_2/\Delta u - \eta\hat{\delta}_\theta) d\hat{K}/d\eta$ , and reminder  $e$  from equation (A 1).

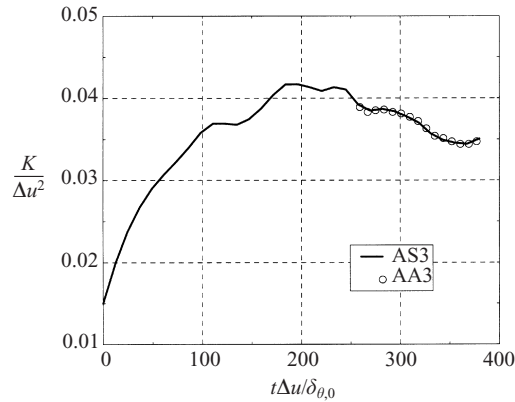


FIGURE 23. Evolution of turbulent kinetic energy at the centreplane for simulations AS3 and AA3 (50% increased resolution).

between successive filter applications. The relative importance of filtering with respect to the physical viscous dissipation is measured by the ratio

$$\frac{k - k^*}{n\epsilon\Delta t}. \quad (\text{A } 2)$$

Thus, an equivalent filter dissipation can be defined by

$$\epsilon_f = \frac{k - k^*}{n\Delta t} \quad (\text{A } 3)$$

and, to preserve the fidelity of the simulations, it is required that  $\epsilon_f/\epsilon$  be small.

Figure 24 shows different measurements of the ratio  $(\epsilon_f/\epsilon)_{max}$  as a function of  $n$  for simulations AS3 and AA3. No further improvement was observed for  $n > 50$  and this value was used in the present study for all simulations. Notice that in cases A3, A7 and A11 the ratio  $\epsilon_f/\epsilon \simeq 6\%$  while  $\epsilon_f/\epsilon \simeq 1\%$  in the higher-resolution case AA3.

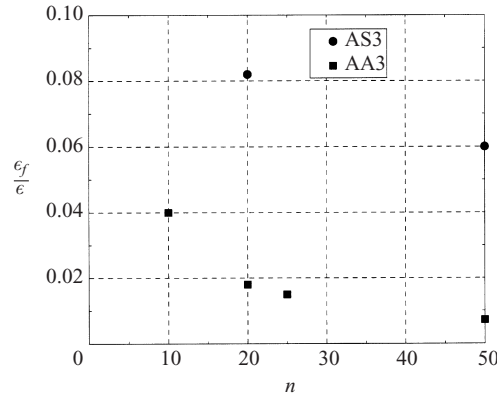


FIGURE 24. Dependence of normalized filter dissipation on  $n$ , the number of time steps between filtering.

There is additional support that the current filter is acceptable. The kinetic energy balance in figure 22 shows that the right- and left-hand sides of the kinetic energy equation are in balance. Furthermore, figure 6 shows that our level of turbulent dissipation is in excellent agreement with the result of Rogers & Moser (1994) even though a completely different numerical scheme was used. For these reasons, it was considered that the value of  $n = 50$  was sufficient for the purpose of the present study.

The effect of the filter on the one-dimensional turbulent kinetic energy spectrum is shown in figure 25(a). As can be seen from the filter transfer function, the filter affects only the larger wavenumbers. Figure 25(b) shows the dissipation spectrum,  $D(\kappa)$ . It can be seen that the filter only affects wavenumbers that are larger than those at which  $D(\kappa)$  peaks.

## Appendix B. Two-time-scale correlation model

Consider the integral to be evaluated in (4.15). Let  $\hat{F}_{ij}(\tau, \mathbf{k}) = \hat{F}_{ij}(\mathbf{k})R(\tau)$  so that (4.15) becomes

$$\Psi_{ij}(\mathbf{k}) = \frac{(2\pi)^3}{2Vk^2} \hat{F}_{ij}(\mathbf{k}) \omega \int_0^\infty R(\tau) \sin(\omega\tau) d\tau, \quad (\text{B } 1)$$

where  $\omega = c_o k$ . To simplify the notation we introduce an intermediate function  $H(\omega)$  such that

$$H(\omega) = \omega \int_0^\infty R(\tau) \sin(\omega\tau) d\tau. \quad (\text{B } 2)$$

It is possible to obtain the asymptotic expansions of  $H(\omega)$  for an arbitrary function  $R(\tau)$  in the limits of small and large  $\omega$ . The only restriction imposed is that the function  $R(\tau)$  must approach zero for  $\tau \rightarrow \infty$ . In the first case, we expand in Taylor series  $\sin(\omega\tau)$  for small values of  $\omega$  and in the second we perform the change of variable  $\zeta = \omega\tau$  and performing integration by parts. The results of the expansions for small  $\omega$  is

$$H(\omega) = \omega^2 \int_0^\infty \tau R(\tau) d\tau - \frac{\omega^4}{3!} \int_0^\infty \tau^3 R(\tau) d\tau + O(\omega^6) \quad (\text{B } 3)$$

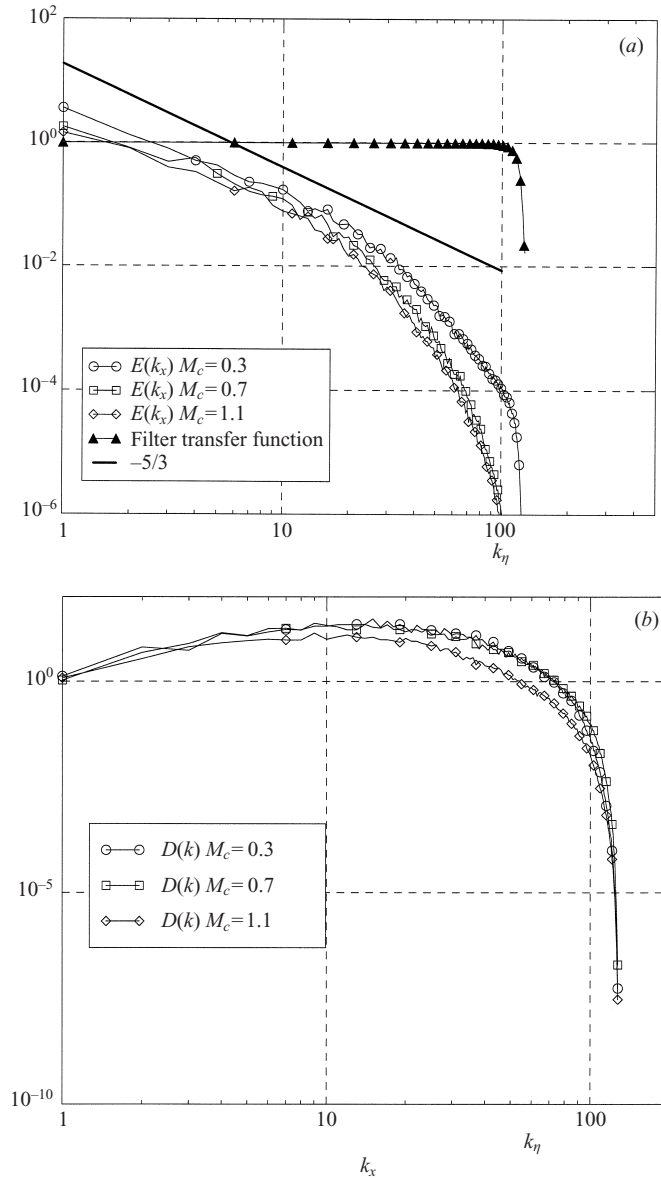


FIGURE 25. One-dimensional spectrum of (a) turbulent kinetic energy and (b) turbulent dissipation at different Mach numbers.

and for large  $\omega$

$$H(\omega) = R(0) - \frac{1}{\omega^2} R''(0) + \frac{1}{\omega^4} R'''(0) + O(\omega^{-6}). \quad (\text{B4})$$

As can be seen, the asymptotic expansions obtained in §4.2 are indeed general for both small and large Mach numbers. Now instead of assuming  $R(\tau) = e^{-\tau/\tau_I}$  we consider the more general case where a viscous time scale,  $\tau_v$ , applies for small  $\tau$ . We will assume high-Reynolds-number turbulence such that, with Kolmogorov scaling,  $\tau_v$  is determined by  $\epsilon$  and  $\nu$ , giving  $\tau_v/\tau_I = Re_I^{-1/2}$ . Thus  $(\tau_v/\tau_I)$  is a small parameter.

There is no reason, *a priori*, to exclude quadratic or linear dependence of  $R(\tau)$  for small  $\tau$  and we will consider both cases.

### B.1. Quadratic viscous dependence

A two-time-scale model for  $R(\tau)$  is considered in which

$$R(\tau) = \begin{cases} e^{-\tau^2/\tau_v^2}, & 0 < \tau < a_1\tau_v \\ Ae^{-\tau/\tau_l}, & a_1\tau_v < \tau < \infty, \end{cases} \quad (\text{B } 5)$$

where  $\tau_v$  and  $\tau_l$  are characteristic time scales of the decorrelation function  $R(\tau)$  such that  $\delta = \tau_v/\tau_l \ll 1$ . The constant  $a_1$  is positive of order unity and the constant  $A$  is obtained from the matching condition

$$A = e^{-a_1^2} e^{a_1\delta}$$

Notice that (B 2) consists of two parts,  $H = H_v + H_l$ , where

$$H_v = \omega \int_0^{a_1\tau_v} e^{-\tau^2/\tau_v^2} \sin(\omega\tau) d\tau,$$

$$H_l = \omega A \int_{a_1\tau_v}^{\infty} e^{-\tau/\tau_l} \sin(\omega\tau) d\tau.$$

Since  $\delta \ll 1$  we proceed to expand these integral in powers of  $\delta$ . The algebra of the asymptotic expansions is omitted here for brevity, but shows that for small values of  $(\omega\tau_l\delta)^2$

$$H_l = \frac{(\omega\tau_l)^2}{1 + (\omega\tau_l)^2} e^{-a_1^2} (1 + a_1\delta + O(\delta^2)), \quad (\text{B } 6)$$

$$H_v = \frac{(\omega\tau_l)^2}{2} (1 - e^{-a_1^2}) \delta^2 + O(\delta^4). \quad (\text{B } 7)$$

From (B 4) the asymptotic expansion for large values of  $\omega$  is

$$H = 1 + \frac{2}{\omega^2\tau_v^2} + O(\omega^{-4}). \quad (\text{B } 8)$$

This shows that one would not expect a decorrelation function that has a quadratic viscous time dependence since this would imply a pressure strain that, for small but non-zero Mach number, is larger than the incompressible value, in contradiction with observations. Furthermore, figure 12 does not support a quadratic viscous dependence.

### B.2. Linear viscous dependence

Now a two-time-scale model for  $R(\tau)$  is considered in which

$$R(\tau) = \begin{cases} e^{-\tau/\tau_\lambda}, & 0 < \tau < a_2\tau_\lambda \\ Be^{-\tau/\tau_l}, & a_2\tau_\lambda < \tau < \infty, \end{cases} \quad (\text{B } 9)$$

where  $\tau_\lambda$  and  $\tau_l$  are characteristic time scales of the decorrelation function  $R(\tau)$  such that  $\epsilon = \tau_\lambda/\tau_l \ll 1$ . Here  $\tau_\lambda$  represents viscous effects. As in the previous case the constant  $a_2$  is positive of order unity and the constant  $B$  is obtained from the matching condition

$$B = e^{-a_2} e^{a_2\epsilon}.$$

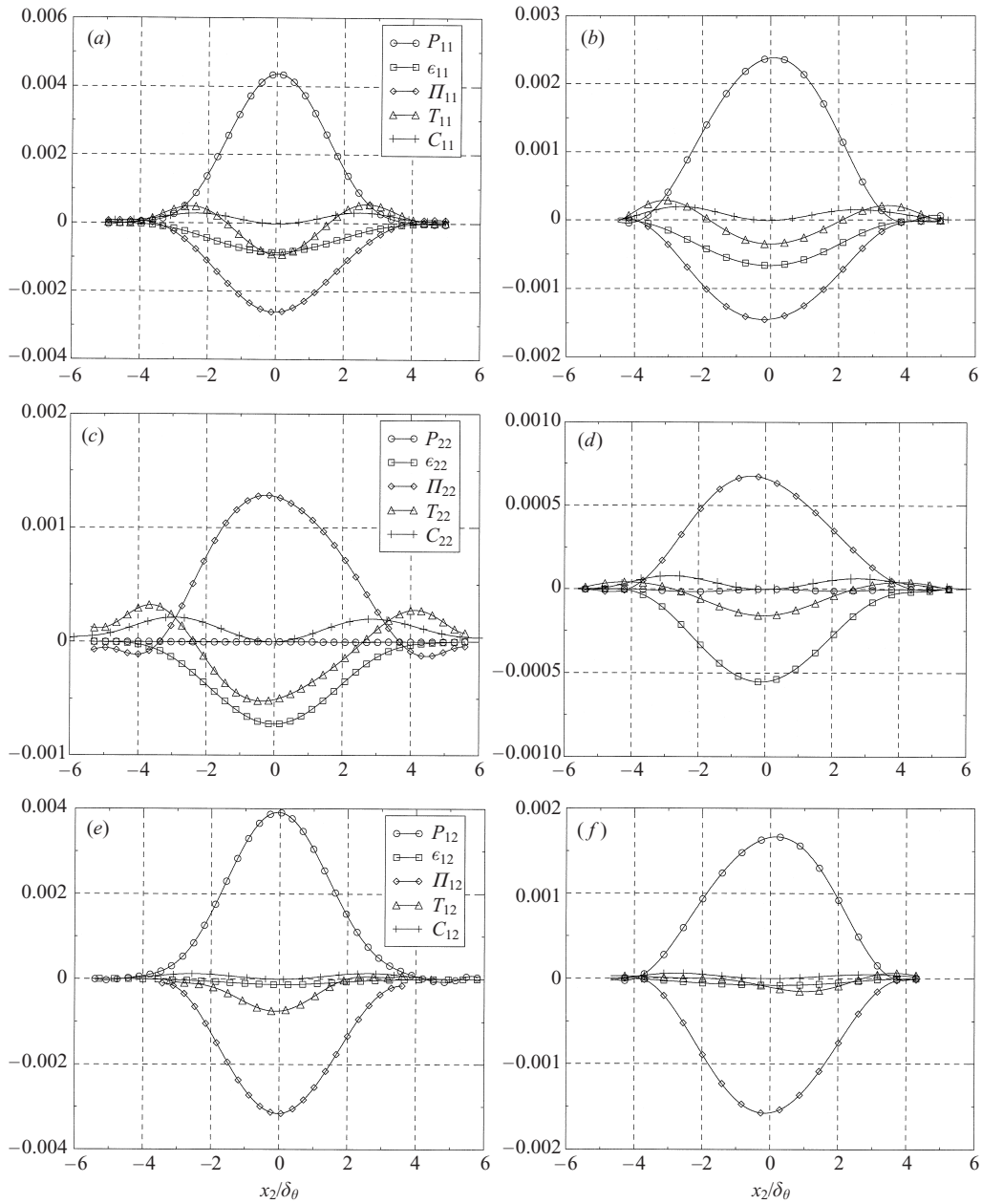


FIGURE 26. Reynolds stress budgets:  $R_{11}$  for (a)  $M_c = 0.3$  and (b)  $M_c = 1.1$ ;  $R_{22}$  for (c)  $M_c = 0.3$  and (d)  $M_c = 1.1$ ;  $R_{12}$  for (e)  $M_c = 0.3$  and (f)  $M_c = 1.1$ . Terms are normalized by  $\Delta U^3/\delta_\theta$ . Production,  $P$ , dissipation,  $\epsilon$ , pressure-strain,  $\Pi$ , transport,  $T$  and time derivative + convection,  $C$ .

As in the previous case,  $H = H_\lambda + H_I$ , where

$$H_\lambda = \omega \int_0^{a_2\tau_\lambda} e^{-\tau/\tau_\lambda} \sin(\omega\tau) d\tau,$$

$$H_I = \omega B \int_{a_2\tau_\lambda}^\infty e^{-\tau/\tau_I} \sin(\omega\tau) d\tau,$$

with corresponding expansions for small values of  $(\omega\tau_I\epsilon)^2$

$$H_I = \frac{(\omega\tau_I)^2}{1 + (\omega\tau_I)^2} e^{-a_2} (1 + a_2\epsilon + O(\epsilon^2)), \quad (\text{B } 10)$$

$$H_\lambda = (\omega\tau_I)^2 \epsilon^2 + O(\epsilon^4), \quad (\text{B } 11)$$

and for large values of  $\omega$

$$H = 1 - \frac{1}{\omega^2\tau_\lambda^2} + O(\omega^{-4}). \quad (\text{B } 12)$$

This expression has the expected behaviour; as we increase the speed of sound ( $\omega \rightarrow \infty$ ) we approach the incompressible value. Equations (B 6)–(B 7) and (B 10)–(B 11) show that the leading-order dependence of the integral is unchanged up to a multiplicative constant for both linear and quadratic choices for the small-time behaviour of the temporal decorrelation function. To conclude, the use of a more complete model that includes viscous effects leads to insignificant changes with respect to the dependence on Mach number given by (4.20).

### Appendix C. Reynolds stress budgets

For completeness, the Reynolds stresses budgets for components  $R_{11}$ ,  $R_{22}$  and  $R_{12}$  are shown at  $M_c = 0.3$  and 1.1 in figure 26. The velocity difference,  $\Delta U$ , is used. All terms in the budget are normalized with  $(\Delta U^3)/\delta_\theta$ .

The balance for the streamwise component in figure 26(*a, b*) shows that, in the core of the shear layer, the dominant source is  $P_{11}$  while the dominant sink is  $\Pi_{11}$  which redistributes energy to the other velocity components. Turbulent dissipation,  $\epsilon_{11}$ , and transport,  $T_{11}$ , also contribute to the balance. Both  $P_{11}$  and  $\Pi_{11}$  are substantially reduced at high Mach number. On the other hand, the dissipation,  $\epsilon_{11}$ , changes less with Mach number.

The balance for the cross-stream component is shown in figure 26(*c, d*). The pressure–strain term,  $\Pi_{22}$ , is the dominant source. Its value decreases substantially at high Mach number. In the  $M_c = 0.3$  case, both dissipation and transport are important sinks near the centreline. At the higher Mach number,  $M_c = 1.1$ , the dissipation,  $\epsilon_{22}$ , has a slight reduction while there is a more substantial reduction in the transport,  $T_{22}$ .

Figure 26(*e, f*) shows the budget for the Reynolds shear stress,  $R_{12}$ . The dominant source is the production while the dominant sink is the pressure–strain correlation. At  $M_c = 1.1$ , both of these terms are reduced with respect to the low-Mach-number case. The dissipation term is negligible, which is consistent with the implication of local isotropy of the turbulent dissipation rate at sufficiently high Reynolds number. The transport term has a small contribution at  $M_c = 0.3$  while it is negligible at  $M_c = 1.1$ .

Overall, the Reynolds stress budgets show that the  $M_c = 1.1$  case exhibits substantial reduction in the production and pressure–strain terms with respect to the baseline case with  $M_c = 0.3$ . The transport terms are also reduced. However, the turbulent dissipation terms are not significantly affected by Mach number.

### REFERENCES

- BALSA, T. F. & GOLDSTEIN, M. E. 1990 On the instabilities of supersonic mixing layers: a high-Mach-number asymptotic theory. *J. Fluid Mech.* **216**, 585–611.

- BARRE, S., QUINE, C. & DUSSUAGE, J. 1994 Compressibility effects on the structure of supersonic mixing layers: experimental results. *J. Fluid Mech.* **259**, 47–78.
- BELL, J. H. & MEHTA, R. D. 1990 Development of a two-stream mixing layer from tripped and untripped boundary layers. *AIAA J.* **28**, 2034–2042.
- BLAISDELL, G. A., MANSOUR, N. N. & REYNOLDS, W. C. 1993 Compressibility effects on the growth and structure of homogeneous turbulent shear flow. *J. Fluid Mech.* **256**, 443–485.
- BOGDANOFF, D. 1983 Compressibility effects in turbulent shear layers. *AIAA J.* **21**, 926–927.
- BRADSHAW, P. 1977 Compressible turbulent shear layers. *Annu. Rev. Fluid Mech.* **21**, 926–927.
- BREIDENTHAL, R. 1990 The sonic eddy – a model for compressible turbulence. *AIAA Paper* 90-0495.
- BROWN, G. 1974 The entrainment and large structure in turbulent mixing layers. *5th Australasian Conf. on Hydraulics and Fluid Mechanics*, pp. 352–359 (ed. D. Lindley, A. J. Sutherland). Canterbury University.
- BROWN, G. L. & ROSHKO, A. 1974 On density effects and large structure in turbulent mixing layers. *J. Fluid Mech.* **64**, 775–816.
- CAMBON, C., COLEMAN, G. N. & MANSOUR, N. N. 1993 RDT and DNS of compressible homogeneous turbulence at finite Mach number. *J. Fluid Mech.* **257**, 641–665.
- CHAMBRES, O., BARRE, S. & BONNET, J. 1998 Detailed turbulence characteristics of a highly compressible supersonic turbulent plane mixing layer. *J. Fluid Mech.* Submitted.
- CLEMENS, N. T. & MUNGAL, M. G. 1995 Large-scale structure and entrainment in the supersonic mixing layer. *J. Fluid Mech.* **284**, 171–216.
- DEBISSCHOP, J. R. & BONNET, J. P. 1993 Mean and fluctuating velocity measurements in supersonic mixing layers. In *Engineering Turbulence Modelling and Experiments 2*. (ed. W. Rodi & F. Martelli). Elsevier Science Publishers.
- DIMOTAKIS, P. 1984 Two-dimensional shear layer entrainment. *AIAA J.* **24**, 1791–1796.
- ELLIOT, G. S. & SAMIMY, M. 1990 Compressibility effects in free shear layers. *Phys. Fluids A* **2**, 1231–1240.
- ERLEBACHER, G., HUSSAINI, M. Y., KREISS, H. O. & SARKAR, S. 1990 The analysis and simulation of compressible turbulence. *Theor. Comput. Fluid Dyn.* **2**, 73–95.
- FREUND, J. B., LELE, S. K. & MOIN, P. 2000 Compressibility effects in a turbulent annular mixing layer. Part 1. Turbulence and growth rate. *J. Fluid Mech.* **421**, 229–267.
- FRIEDRICH, R. & BERTOLLOTTI, F. P. 1997 Compressibility effects due to turbulent fluctuations. *Appl. Sci. Res.* **57**, 165–194.
- GOEBEL, S. G. & DUTTON, J. C. 1991 Velocity measurements of compressible, turbulent mixing layers. *AIAA J.* **29**, 538–546.
- GRUBER, M., MESSERSMITH, N. & DUTTON, J. 1993 Three-dimensional velocity field in a compressible mixing layer. *AIAA J.* **31**, 2061–2067.
- HALL, J. L., DIMOTAKIS, P. E. & ROSEMAN, H. 1993 Experiments in nonreacting compressible shear layers. *AIAA J.* **31**, 2247–2254.
- KLINE, S. J., CANTWELL, B. J. & LILLEY, G. M. 1982 *Proc. 1980-81-AFOSR-HTTM-Stanford Conf. on Complex Turbulent Flows*, vol. 1. Stanford University Press.
- LELE, S. K. 1992 Compact finite differences schemes with spectral-like resolution. *J. Comput. Phys.* **103**, 16–42.
- LELE, S. K. 1994 Compressibility effects on turbulence. *Annu. Rev. Fluid Mech.* **26**, 211–254.
- LU, G. & LELE, S. K. 1994 On the density effects on the growth rate of compressible mixing layer. *Phys. Fluids* **6**, 1073–1075.
- MORKOVIN, M. V. 1987 Transition at hypersonic speeds. *ICASE Interim Rep.* 1.
- PAPAMOSCHOU, D. & LELE, S. K. 1993 Vortex-induced disturbance field in a compressible shear layer. *Phys. Fluids A* **5**, 1412–1419.
- PAPAMOSCHOU, D. & ROSHKO, A. 1988 The compressible turbulent shear layer: an experimental study. *J. Fluid Mech.* **197**, 453–477.
- RISTORCELLI, J. R. 1997 A pseudo-sound constitutive relationship for the dilatational covariances in compressible turbulence. *J. Fluid Mech.* **347**, 37–70.
- ROGERS, M. M. & MOSER, R. D. 1994 Direct simulation of a self-similar turbulent mixing layer. *Phys. Fluids* **6**, 903–923.
- SAMIMY, M. & ELLIOT, G. S. 1990 Effects of compressibility on the characteristics of free shear layers. *AIAA J.* **28**, 439–445.

- SAMIMY, M., REEDER, M. F. & ELLIOTT, G. S. 1992 Compressibility effects on large structures in free shear flows. *Phys. Fluids A* **4**, 1251–1258.
- SANDHAM, N. D. & REYNOLDS, W. C. 1991 Three-dimensional simulation of large eddies in the compressible mixing layer. *J. Fluid Mech.* **224**, 133–158.
- SARKAR, S. 1992 The pressure-dilatation correlation in compressible flows. *Phys. Fluids A* **4**, 2674–2682.
- SARKAR, S. 1995 The stabilizing effect of compressibility in turbulent shear flow. *J. Fluid Mech.* **282**, 163–186.
- SARKAR, S. 1996 On density and pressure fluctuations in uniformly sheared compressible flow. In *Proc. IUTAM Symp. on Variable Density Low-Speed Flows, Marseille, July 1996* (ed. L. Fulachier, J. L. Lumley & F. Anselmet).
- SARKAR, S., ERLEBACHER, G., HUSSAINI, M. Y. & KREISS, H. O. 1991 The analysis and modeling of dilatational terms in compressible turbulence. *J. Fluid Mech.* **227**, 473–493.
- SIMONE, A., COLEMAN, G. N. & CAMBON, C. 1997 The effect of compressibility on turbulent shear flow: a rapid-distortion-theory and direct-numerical-simulation study. *J. Fluid Mech.* **330**, 307–338.
- SMITS, A. & DUSSAUGE, J. P. 1996 *Turbulent Shear Layers in Supersonic Flows*. American Institute of Physics Press.
- SPENCER, B. W. & JONES, B. G. 1971 Statistical investigation of pressure and velocity fields in the turbulent two-stream mixing layer. *AIAA Paper* 71-613.
- TAULBEE, D. & VANOSDOL, J. 1991 Modeling turbulent compressible flows: the mass fluctuating velocity and squared density. *AIAA Paper* 91-0524.
- THOMPSON, K. W. 1987 Time dependent boundary conditions for hyperbolic systems. *J. Comput. Phys.* **68**, 1–24.
- VREMAN, A. W., SANDHAM, N. D. & LUO, K. H. 1996 Compressible mixing layer growth rate and turbulence characteristics. *J. Fluid Mech.* **320**, 235–258.
- WILLIAMSON, J. K. 1980 Low-storage Runge-Kutta schemes. *J. Comput. Phys.* **35**, 48–56.
- WYGNANSKI, I. & FIEDLER, H. E. 1970 The two-dimensional mixing region. *J. Fluid Mech.* **41**, 327–361.
- ZEMAN, O. 1990 Dilatational dissipation—the concept and application in modelling compressible mixing layers. *Phys. Fluids A* **2**, 178–188.